FORSCHUNGSZENTRUM JÜLICH GmbH

Institut für Festkörperforschung

Spin-Resolved Photoemission from Pd on Fe(100)

Oliver Rader

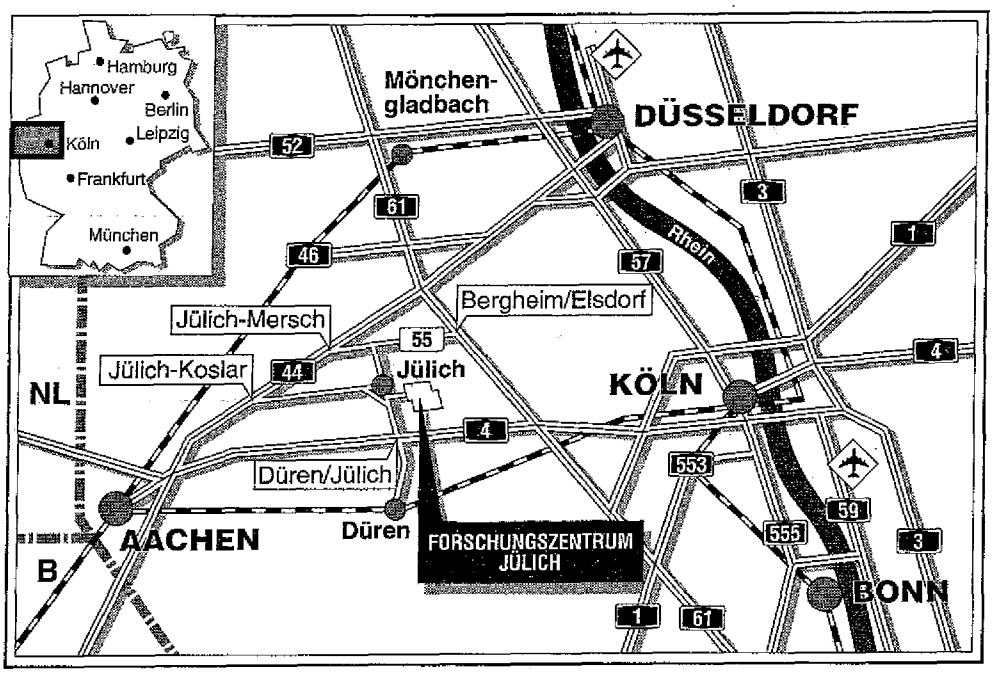

Berichte des Forschungszentrums Jülich ; 2558
ISSN 0366-0885
Institut für Festkörperforschung Jül-2558

Zu beziehen durch: Forschungszentrum Jülich GmbH · Zentralbibliothek
Postfach 1913 · D-5170 Jülich · Bundesrepublik Deutschland
Telefon: 02461/61-6102 · Telefax: 02461/61-6103 · Telex: 833556-70 kfa d

Spin-Resolved Photoemission from Pd on Fe(100)

Oliver Rader

Contents

"Sollte nicht schon bloße *Berührung* mancher Körper mit Eisen [sie] ebenso anziehbar für den Magneten machen...
Wird Eisen mit verschiedenen Substanzen in Berührung wohl verschieden vom Magnet gezogen?"

Johann Wilhelm Ritter (1800)[1]

1. Introduction

The properties of *ultrathin* magnetic films* are an object of current experimental and theoretical research as they permit to study the evolution of the co-operative effect *ferromagnetism* in the transition range from two- to three-dimensionality.

The realization of ultrathin metal films has become possible by progress in preparation techniques, involving *molecular beam epitaxy* (MBE) and improved *ultrahigh vacuum* (UHV) conditions, and in characterization methods like *Auger electron spectroscopy* (AES), *low-energy electron diffraction* (LEED), or *scanning tunneling microscopy* (STM), which allows to monitor the quality of a sample even on an atomic scale.

The questions for the existence of monolayer ferromagnetism, the size of magnetic moments in ultrathin layers in relation to bulk values, enhancement or absence of magnetism at bulk surfaces and the strength and direction of coupling between ferromagnetic or antiferromagnetic layers in sandwiches or multilayer systems have been addressed in this field. Among the prominent results that have been achieved hitherto are the experimental proof of ferromagnetism in *monolayers* of Fe on Au(100)[2] and Co on Au(100)[3].

Currently there is considerable ambition to find a bulk paramagnet which becomes ferromagnetic as an ultrathin film on an appropriate substrate. For reasons pointed out below an *ultrathin layer of palladium on top of the (100) face of iron* is expected to show strong tendencies to become ferromagnetic.

While for the study of a ferromagnetic layer on top of a dia- or paramagnetic substrate averaging as well as local methods of measurement† are applied, the

---

* In general films that are not more than ≈4 atomic layers thick are referred to as "ultrathin".

† Measurement methods of thin-film magnetism are: *(1)* Highly sensitive magnetometry methods, which measure an averaged magnetic moment, like the *vibrating sample magnetometer*, the *torsion oscillation magnetometer*, the *Faraday balance*, and the *superconduction quantum interference device* (SQUID), *(2)* the *surface magneto-optical Kerr effect* (SMOKE) and the *Brillouin light scattering* gaining magnetic information from a region extending only some 100 Å from the surface into the bulk due to the penetration depth of light in metals, *(3)* the *Mössbauer spectroscopy*, site and element specific as the probe, certain isotopes out of a limi-

system Pd/Fe(100) requires a method that is *surface and element specific*. This specification is fulfilled by the *spin-resolved photoelectron spectroscopy* or *spin-resolved photoemission* which is in so far unique as it provides information on both magnetism and electronic structure and is surface sensitive when performed at sufficiently low energies.

Whilst the Pd *atom* has the outer electron configuration $4d^{10}5s^0$, in the *solid* the electrons rearrange and charge is transferred to form[4] $4d^{8.722}5s^{0.620}5p^{0.658}$ and convert the diamagnetic free atoms to a metal with an extraordinaryly large paramagnetic susceptibility[5]. The paramagnetic susceptibility is exchange-enhanced[6] and the density of states at the Fermi edge $n(E_F)$, as it results from slab calculations[7,8], multiplied by the exchange integral[9,10] yields[8] $n(E_F) \cdot I \approx 0.9$ and thus misses the Stoner criterion for ferromagnetism by only 10%.

Additionally, for the Pd *surface layer* a strongly enhanced susceptibility (with respect to the bulk) has been calculated[12], but surface ferromagnetism was found to be absent in theory[8].

On the other hand it is known that contact between Pd and 3*d* transition metal impurites in dilute Pd alloys produces *giant moments* of e. g. $\approx 12\mu_B$ for *Pd*Fe and $\approx 11\mu_B$ for *Pd*Co.[13,14] The giant moment consists of the impurity moment itself plus a polarization cloud which extends for about 10 Å inducing a moment of approximately $0.05\mu_B$ on some 200 Pd atoms.[15]

FePd alloys in a more balanced compositional regime are ferromagnetic with an averaged magnetic moment per atom decreasing from $\approx 2\mu_B$ at 30% Pd to $\approx 1\mu_B$ at 80% Pd[16].

For obvious reasons polarization effects similar to giant moment magnetism are expected at two-dimensional 3*d* metal-Pd interfaces. *Hillebrands et al.*[17], using Brillouin spectroscopy and a SQUID magnetometer, observe a magnetic polarization of the Pd spacer layers in sputtered Fe/Pd superlattices (thickness of each layer between 33 and 188 Å).

In a theoretical study of 3*d* transition metal overlayers on Pd(100) *Blügel*[8,11] finds that one monolayer of Fe, Co, and Ni is ferromagnetic on Pd(100). The magnetic moment in the Fe monolayer is enhanced by $1\mu_B$. Additionally, a magnetic moment of $0.32\mu_B$ is induced on the atoms of the topmost Pd layer and still $0.17\mu_B$ on the succeeding Pd layer.[8,11] The occupation of the 4*d* subshell in Pd metal limits the induced magnetic moment to $0.36\mu_B$ and the difference between this value and that found in the giant moment case is due to the difference in the

---

ted number of elements, can be placed at any desired location during the production of the sample, *(4)* methods sensitive to the magnetism only in the topmost atomic layers like *spin-polarized low-energy electron diffraction* (SPLEED) and *electron capture spectroscopy*, and *(5)* the surface sensitive energy spectroscopy methods *spin-polarized inverse photoemission* and *spin-resolved (ultraviolet) photoelectron spectroscopy*.

number of next neighbors.[8] A saturation of the Pd magnetic moment is found for a PdFe alloy at 16% Fe.[18]

Contrasting results have been reported by *Hosoito et al.*[19,20], who studied the magnetism of Fe-Pd interfaces by ^{57}Fe Mössbauer spectroscopy thus probing the hyperfine field at the Fe sites. They conclude the first Fe layer in contact with Pd to be paramagnetic at room temperature. Polarized neutron diffraction measurements performed by the same group[21] seem to support this conclusion. Nevertheless, crystallographical information is missing[19], and similar results (reduction of the magnetization in the first Fe layer at the interface by 30%) for Fe-V multilayers[22] can also be interpreted taking into account a non-rectangular composition profile[23] due to alloying.

Recent theoretical calculations[25,26,27] predict that a lattice expansion by 5 to 6% will render Pd ferromagnetic because of the sensitive dependence of the s-d hybridization on the lattice constant. An enhanced susceptibility had been experimentally found already for Pd stretched in Au/Pd/Au sandwiches[28] due to band-narrowing and thereby increased density of states at E_F. With electron capture spectroscopy *Rau*[29] finds ferromagnetism in up to 10 monolayers of lattice expanded Pd on Ag(100), nevertheless, magneto-optic Kerr effect measurements[30] do not show ferromagnetism in this system.

The theoretical predictions[25,26,27] together with a report by *Hillebrands et al.*[31] on the observation of induced moments at the interfaces also of epitaxially grown Fe(110)/Pd(111) superlattices have motivated *Celinski et al.*[32] to grow Pd on Fe on Ag(100) in order to expand the Pd lattice constant by 5.1%. Reflection high-energy electron diffraction (RHEED) together with the exponential decay of the Fe Auger signal lets them conclude that the lateral lattice spacing in the Pd is the same as that of the substrate.[32] In ferromagnetic resonance (FMR) and Brillouin scattering they find that four Pd layers sandwiched between Fe are ferromagnetic while five layers are not. *Celinski et al.* try to distinguish between the magnetic properties of the Fe/Pd interface in Ag/5Fe/8Pd/20Au (numbers denote monolayers) and those of the Fe substrate by comparison with a Pd-free reference sample and conclude that an extra magnetic moment of $0.9\mu_B$/atom is created. The report of *Celinski et al.* has been the starting point for the present work.

The work is organized as follows: In chap. 2.1 the preparation of the Fe substrate and the Pd overlayers will be described. Then, in view of the possibility of interdiffusion between Fe and Pd and the fact that FePd alloys behave ferromagnetically in a wide compositional regime a careful study of the growth mode of Pd on Fe(100) must follow in chap. 2.2 and chap. 2.3. After a compilation of theoretical and technical aspects of photoelectron spectroscopy in chap. 3 the results of spin- and angle-resolved photoemission are presented and discussed in comparison with a band structure calculation in chap. 4. Chap. 5 gives a summary of this work.

2. Sample preparation and characterization

2.1. Sample preparation

The picture frame shaped Fe(100) 3%Si single crystal has been prepared *in situ* by Ne^+-sputtering at 2 keV and heating. In order to achieve minimum surface roughness the crystal was flashed to 370°C for 2 min. Although after this treatment no surface segregation of Si was detectable by Auger electron spectroscopy, 5 to 10 ML of Fe have been evaporated onto the crystal prior to Fe photoemission as well as prior to Pd overlayer preparation. Fe and Pd were evaporated by electron beam heating from 99.999% resp. 99.994% purity wires at a rate of typically 0.17 ML/min with the evaporating facilities surrounded by water-cooled jackets to prevent contamination by thermal desorption. The sample was held at room temperature during evaporation to prevent interdiffusion. The evaporation rates were measured with the use of a quartz crystal microbalance. The basic pressure of the chamber was $1.8 \cdot 10^{-10}$ mbar and raised during evaporation to $6 \cdot 10^{-10}$ mbar. Data acquisition time for spin-resolved spectra was typically 1 h. In general, each sample has been used only for one spin-resolved spectrum and was sputtered afterwards. An exception is the determination of the Pd coverage at which the spin polarization vanishes. In this case the overlayer thickness has been increased successively. Nevertheless, it was found that both procedures yield the same spectra with respect to shape and polarization.

2.2. Application of Auger electron spectroscopy

2.2.1. The Auger process

The emission of an *Auger* electron with characteristic kinetic energy E by an atom can in the simplest case be understood as a two-step process involving three atomic levels. This is reflected by the common notation XYZ for Auger electrons. In the first step a hole is created in the core level X by incident electrons, photons, or ions. In the second step an electron of a higher level Y fills this hole. The energy gained by that is emitted in two competing processes. Either characteristic X-rays are emitted or the energy is transferred to another electron of level Z which leaves the solid as an Auger electron of kinetic energy E.

Important is the fact that this energy transfer occurs by Coulomb interaction and thus is truly radiationless, so that it is not governed by the selection rules for dipole radiation. E has generally been regarded to be independent from the conditions of the ionization in the first step, an assumption that must be doubted after latest experimental results[33].

2.2.2. The technique of Auger electron spectroscopy

The use of *Auger electron spectroscopy* (AES) in surface analysis is based on its surface and element sensitivity. In the range from 10 eV to 1 keV the *inelastic mean free path* (IMFP) of electrons is in most elements between 3 and 20 Å.[34,35]

It took 40 years from the first observation of Auger electrons by *Pierre Auger*[36] 1925 until the application of AES in surface analysis. *Harris*[37] performed the differentiation of Auger spectra by potential modulation of the analyzer and phase-sensitive amplification, and *Peria* realized that for this the electron gun and the analyzer optics of a conventional LEED system* can be used.[38]

An Auger spectrometer on the basis of a LEED system works as a *retarding field analyzer* (RFA), where a decelerating potential in front of the collector holds back those electrons whose kinetic energy is less than the pass energy. Today the LEED-RFA consists of four grids, which are arranged concentrically in front of the LEED screen, which serves as a collector. The inner grids are both connected to the decelerating potential in order to diminish the lense effect of the mashes of the single grid. The outer grids are grounded in order to keep the area in front of the sample fieldless and to screen the collector from the modulation on the grids. Because all electrons with higher energy can overcome the potential barrier, the retarding field analyzer is a high-pass filter. Thus a first differentiation of the current on the collector in the lock-in amplifier yields the energy distribution curve (A) and a successive differentiation yields its derivative (B). In spectrum B the

---

* LEED (low-energy electron diffraction) will be treated in chap. 2.3.

peak-to-peak heights are proportional to the intensities, i. e. the areas underneath the peaks, in spectrum A. This holds exactly if the peaks in spectrum A are of Gaussian shape. A quantitative comparison of peak-to-peak heights in spectra from different spectrometers requires besides identical peak shapes the same resolution of the spectrometers and the same modulation as well as identical primary electron energy.

2.2.3. Epitaxy

Though often used throughout the literature on thin films, for the use of the term "epitaxy" no standard convention exists[39]. The greek $\epsilon\pi\iota\tau\alpha\xi\iota\varsigma$ means *imposition, direction, arrangement, order, command,* and there is accordance that epitaxy should mean the growth of a material on top of another while adopting the structure of the latter.

We will denote with "epitaxy" in a strict sense the presence of three conditions: *(1)* layer by layer growth, *(2)* perfect order within the layers with the in-plane lattice constant of the substrate, and *(3)* a sharp interface between the substrate and the adsorbate.

In reality deviations from this ideal case occur: island growth, loss of order at higher coverage, and interdiffusion between substrate and adsorbate atoms. The real growth mode can coincide with the ideal case in either one of the listed aspects and deviate from it in another, giving rise to a large number of possible growth modes. Additionally, in many cases a change in the experimental conditions like the order, purity, and temperature of the substrate and the deposition rate of the adsorbate atoms can alter the growth mode of a certain substrate-adsorbate system radically.

2.2.4. Growth modes

In the following we will consider different models for adsorbate growth and in how far they can be distinguished with AES.

If the binding of the adsorbate atoms to the substrate is stronger than that among each other, the *layer by layer* or *Frank-Van der Merwe*[40] growth mode occurs, where the substrate is being covered totally by the first atomic layer of the adsorbate, and each following atomic layer is not begun until the underlying one is completed (Fig. 1 a). Examples are Fe/Au(100)[41] and Co/Cu(100)[41].

During *Volmer-Weber* growth[42] the adsorbate atoms form clusters on the substrate surface, which become, with increasing number of atoms added, three-dimensional islands. As a result, in each stage of the growth process (with respect to *ultrathin* films) large areas of the substrate remain uncovered (Fig. 1 b). The *Volmer-Weber* growth mode occurs if the binding among the adsorbate atoms is

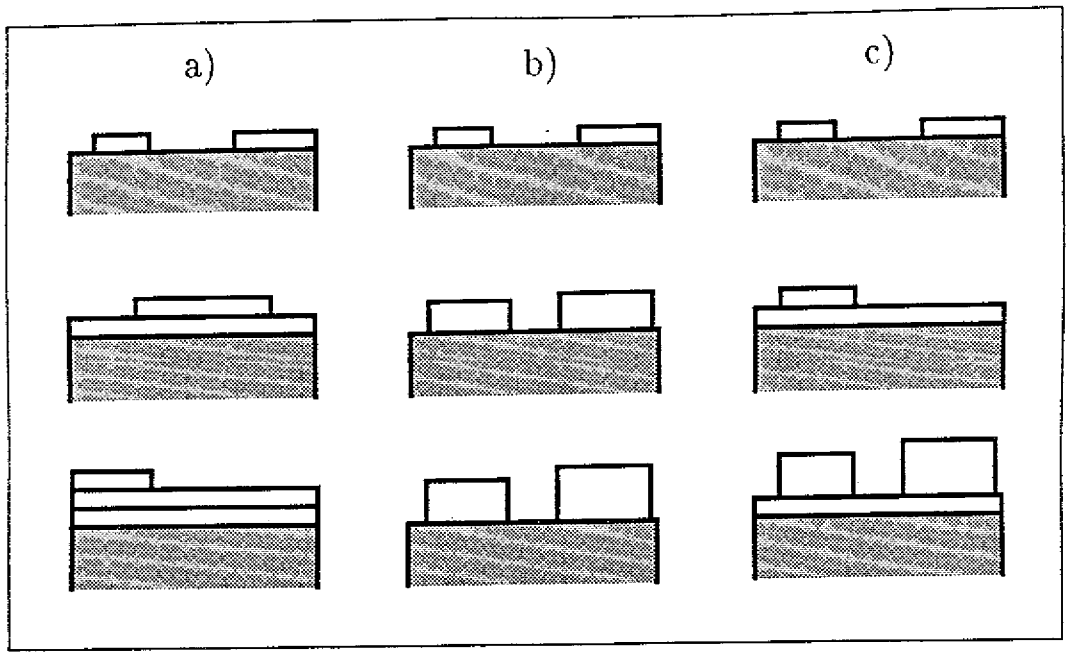

Fig. 1: Compilation of (a) the *layer by layer* or *Frank-Van der Merwe* growth mode, (b) the *island* or *Volmer-Weber* growth mode, and (c) the *layer plus islands* or *Stranski-Krastanov* growth mode.

stronger than that with the substrate. *Volmer-Weber* growth has been found e. g. for Au/NaCl[43] and Pt/Au(100)[44].

Also during the *Stranski-Krastanov* growth[45] three-dimensional crystallites are formed. However, this island growth is preceeded by a complete coverage of the substrate by one (more seldom two) atomic adsorbate layer (Fig. 1 c). Whilst during *Frank-Van der Merwe* growth the binding energy between the adsorbate atoms decreases from the first layer until the bulk value at higher layers, it increases during *Stranski-Krastanov* growth from the second layer on.[46] A reason for this and thus for the "switching" to a different growth mode can for instance be that the lattice constant of the substrate cannot be adopted in the adsorbate ***bulk*** crystal. Examples for *Stranski-Krastanov* behavior are Pd/W(110) (annealed)[47,48] and Pb/Cu(100)[49].

2.2.5. Simulation of growth modes for Auger analysis

Surface analysis with AES averages in contrast to electron microscopy over a macroscopic surface area. Yet, distinction between e. g. island and layer by layer growth is possible.

First, in the Auger spectrum the peaks characteristic of the substrate and the adsorbate material are identified. Then their heights are plotted versus the deposited mass, that is versus time if the adsorbate is successively evaporated with constant evaporation rate onto the clean substrate. In general, the adsorbate si-

gnal will, starting from zero, increase monotonously with the number of deposited atoms whilst the substrate signal will be diminished by the attenuation in the overlayers.

A quantitative model of this behavior of the two signals is based on the following assumptions[50]:

(1) The number of Auger electrons that leave the crystal depends exponentially on the thickness of the traversed film:

$$I = I_0\, e^{-d/\lambda} \tag{1}$$

To get the attenuation α of the Auger signal in one monolayer we insert its d_0 in Eq. 1. For reason of simplicity d_0 denotes the thickness of a monolayer of the *substrate*. Thus we consider the attenuation in the substrate and the adsorbate to be equal.

(2) The parameter λ in Eq. 1 is the *inelastic mean free path* (IMFP) of the electrons. Its dependence on the material and the kinetic energy of the electrons is described by the universal formula given by *Seah* and *Dench*[34,35]:

$$\lambda[\mathrm{nm}] = 0.41\,(a[\mathrm{nm}])^{3/2}\sqrt{E[\mathrm{eV}]} \tag{2}$$

The matter constant a denotes the size of the atoms in the traversed region.* Also here we take the Pd value (0.245 nm). Consequently, instead of regarding four different λ's (the IMFP of Auger electrons deriving from substrate or adsorbate attenuated in the substrate or adsorbate) we only have to deal with two values: the IMFP of electrons originating in the substrate λ_s and the adsorbate λ_a scattered in an averaged attenuating material.

(3) As a consequence of *(2)* the only difference between λ_s and λ_a is the characteristic kinetic energy of the Auger electrons E as it appears in Eq. 2. By inserting d_0 in Eq. 1 we get the attenuation of the Auger signal deriving from the adsorbate $\alpha_a = \exp(-d_0/\lambda_a)$ as well as from the substrate $\alpha_s = \exp(-d_0/\lambda_s)$ in one monolayer of the overlying material.

The different growth modes require different parametrizations of the adsorbate coverage. Let b be the deposition in ML†. Then in case of *Frank-Van der Merwe* growth the number h of completed layers is equal to the integer part of b; the covered fraction x ($x \leq 1$) of the $h+1^{\mathrm{st}}$ layer is the non-integer part of b:

$$h = [b]$$
$$x = b - [b]$$

---

* a is defined in Ref. 34 independently of the crystal structure as $a^3 = 10^{24}\, A/\rho N_A$ with the density ρ[kg/m^3], the atomic weight A, and the Avogadro number N_A.

† We denote with "ML" the mass equivalent of one monolayer of deposited material, independently of the growth mode, as it can be measured for instance with a quartz crystal microbalance.

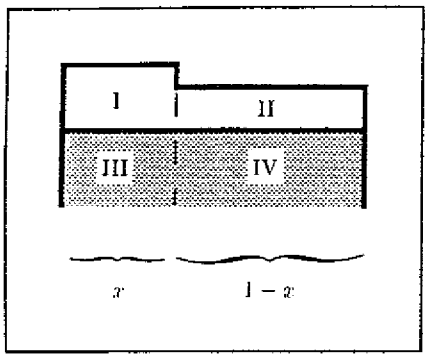

Fig. 2: Schematical view of *Frank-Van der Merwe* growth. h adsorbate layers are completed (h=2). A fraction x of the surface is already covered by the $h+1^{st}$ layer.

By summing up the contributions of all overlayers (Fig. 2) we get the adsorbate signal

$$I_{a,FM} = \underbrace{I_{0a}\, x \sum_{i=0}^{h} \alpha_a^i}_{\text{I}} + \underbrace{I_{0a}\,(1-x) \sum_{i=0}^{h-1} \alpha_a^i}_{\text{II}}.$$

Performing the sum operations yields

$$I_{a,FM} = I_{0a} \left(\frac{1-\alpha_a^h}{1-\alpha_a} + x\alpha_a^h \right).$$

For the semi-infinite substrate crystal the contributions of all layers are summed up as well. The penetration of the electrons through the adsorbate layers is taken into accout by a factor α^{h+1} resp. α^h:

$$I_{s,FM} = \underbrace{I_{0s}\, x \left(\sum_{i=0}^{\infty} \alpha_s^i \right) \alpha_s^{h+1}}_{\text{III}} + \underbrace{I_{0s}\,(1-x) \left(\sum_{i=0}^{\infty} \alpha_s^i \right) \alpha_s^h}_{\text{IV}}$$

After summation we get

$$I_{s,FM} = I_{0s}\, \alpha_s^h \left(\frac{1}{1-\alpha_s} - x \right).$$

A plot of $I_{a,FM}$ and $I_{s,FM}$ versus deposition produces curves of polygonal shape, whose kinks indicate the completion of each atomic layer.* (Fig. 3)

For the *Volmer-Weber* growth we assume that on a fixed area of the substrate islands of rectangular shape and mean height h grow. The parametrization is thus

$$x = \text{const.}$$
$$h = b/x.$$

---

* An experimental observation of these kinks can be found in Ref. 51.

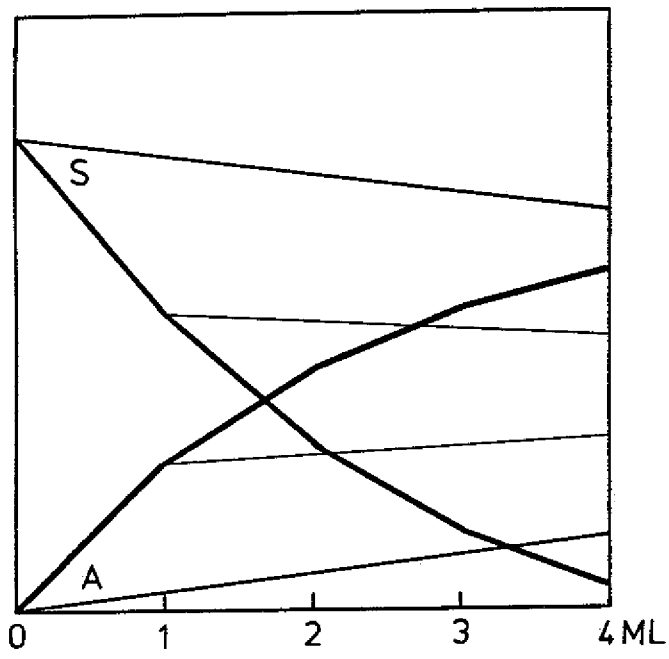

Fig. 3: Schematic behavior of the Auger signals of the substrate (S) and adsorbate (A) as a function of the deposited mass in ML for layer by layer (*Frank-Van der Merwe*) growth (thick line), island (*Volmer-Weber*) growth (medium line), and layer plus island (*Stranski-Krastanov*) growth (thin line).

The contribution of the islands is

$$I_{a,VW} = I_{0a}\, x \sum_{i=0}^{h-1} \alpha_a^i$$
$$= I_{0a}\, x\, \frac{1-\alpha_a^h}{1-\alpha_a}.$$

The non-shadowed and the shadowed parts of the substrate produce

$$I_{s,VW} = I_{0s}\, x \left(\sum_{i=0}^{\infty} \alpha_s^i \right) \alpha_s^h + I_{0s}\,(1-x) \sum_{i=0}^{\infty} \alpha_s^i$$
$$= I_{0s} \frac{1}{1-\alpha_s} (1 + x\alpha_s^h - x).$$

Plotting $I_{a,VW}$ and $I_{s,VW}$ versus deposition shows that the increase of $I_{a,VW}$ and especially the decrease of $I_{s,VW}$ is not as large as with *Frank-Van der Merwe* growth. This is not surprising in view of the uncovered substrate areas given by $x - 1$. The limit $x \longrightarrow 1$ approaches layer by layer growth.

As *Stranski-Krastanov* growth can be regarded as a combination of layer and island growth, for the first layer the relationships of the *Frank-Van der Merwe* growth hold true. From the completion of the first layer on, the parametrization is analogous to the *Volmer-Weber* growth

$$x = \text{const.}$$

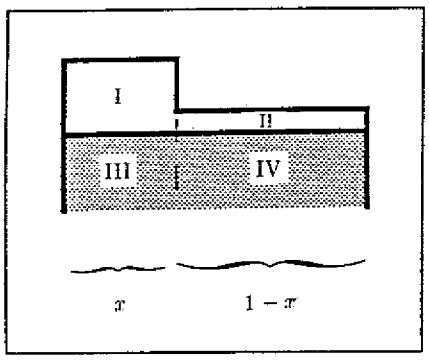

Fig. 4: Schematical view of *Stranski-Krastanov* growth. After completion of one adsorbate layer islands grow continuously, covering a fixed fraction x of the surface.

$$h = \frac{b-1}{x}$$

and the intensity of the adsorbate signal (Fig. 4) becomes

$$\begin{aligned} I_{a,SK} &= \underbrace{I_{0a}\, x \sum_{i=0}^{h} \alpha_a^i}_{\text{I}} + \underbrace{I_{0a}\,(1-x)}_{\text{II}} \\ &= I_{0a}\left(x\,\frac{1-\alpha_a^{h+1}}{1-\alpha_a} + 1 - x\right). \end{aligned}$$

For the substrate we get

$$\begin{aligned} I_{s,SK} &= \underbrace{I_{0s}\, x \left(\sum_{i=0}^{\infty} \alpha_s^i\right) \alpha_s^{h+1}}_{\text{III}} + \underbrace{I_{0s}\,(1-x)\left(\sum_{i=0}^{\infty} \alpha_s^i\right) \alpha_s}_{\text{IV}} \\ &= I_{0s}\frac{\alpha_s}{1-\alpha_s}\,(x\alpha_s^h + 1 - x). \end{aligned}$$

A distinct kink in both curves marks the transition from layer by layer to island growth[46] (Fig. 3).

The results presented so far were adapted from the work of *Ossicini et al.*[50] who discuss the use of AES for the determination of growth modes. These models have in common that they are based on the assumption that the substrate remains unchanged by the adsorbate growth, i. e. diffusion at the interface is ruled out. However, if the binding of the adsorbate to the substrate is strong enough to aim at a high coordination between each other, the adsorbate will diffuse into the substrate and form a three-dimensional alloy. ***With the help of three additional models shall be tested if such an interdiffusion could occur with the system Pd/Fe(100) and if and to what extent it can be recognized with AES.***

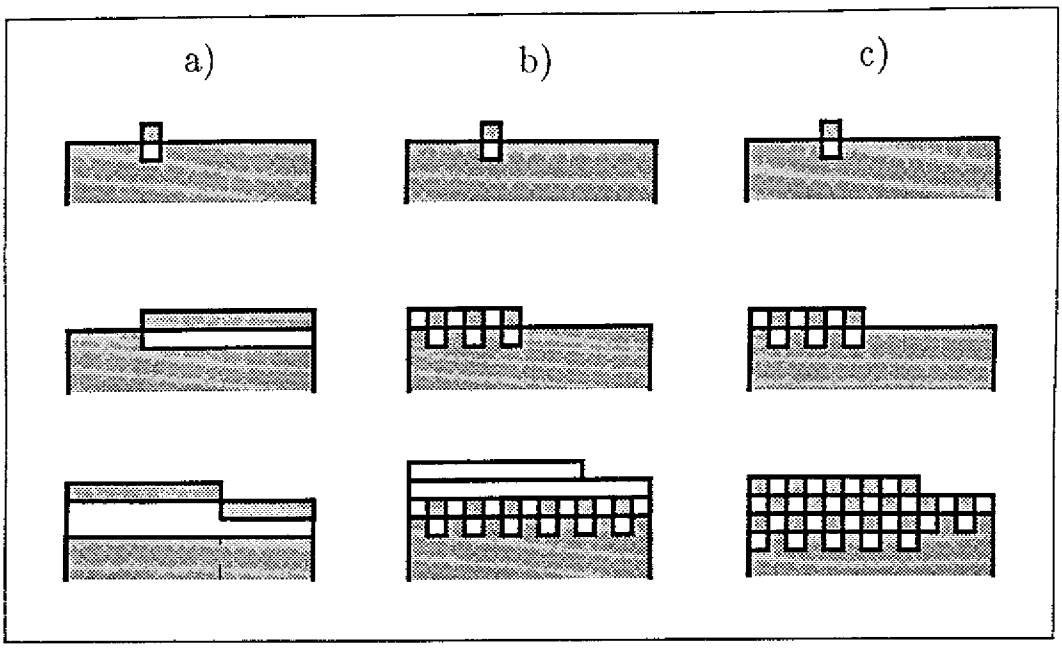

Fig. 5: Growth modes that do not leave the substrate unchanged. (a) Layer by layer growing adsorbate that remains always covered by one layer of atoms from the substrate. (b) Alloying of the *first* deposited ML is simulated in the following way: Every second atom that hits the substrate surface exchanges its place with that of the underlying substrate atom. After one ML of the adsorbate is deposited and thus two layers of alloy are formed the adsorbate grows without further interdiffusion and layer by layer. (c) Three-dimensional alloying. The first deposited ML grows like in (b). Then the alloying continues with every second adsorbate atom exchanging its place with that of a substrate atom.

A first example shall be a growth mode where the growing adsorbate remains permanently covered by one atomic layer formed by atoms from the substrate. The model for this growth (which has been observed for Rh/Ag) becomes apparent from Fig. 5 a).

The parameters are again

$$h = [b]$$
$$x = b - [b].$$

For the adsorbate we get the behavior of the *Frank-Van der Merwe* growth, but attenuated by a constant factor α_a (Fig. 6):

$$I_a = \underbrace{I_{0a}\, x \left(\sum_{i=0}^{h} \alpha_a^i \right) \alpha_a}_{\mathrm{I}} + \underbrace{I_{0a}\,(1-x) \left(\sum_{i=0}^{h-1} \alpha_a^i \right) \alpha_a}_{\mathrm{II}}$$
$$= I_{0a}\, \alpha_a \left(\frac{1-\alpha_a^h}{1-\alpha_a} + x\alpha_a^h \right).$$

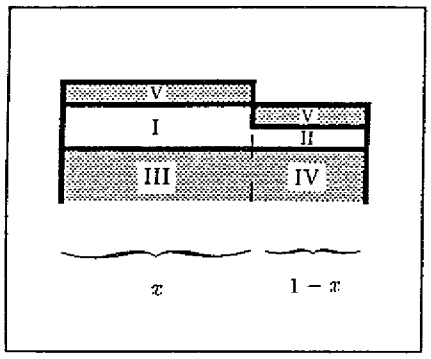

Fig. 6: One substrate layer on top of a layer by layer growing adsorbate. One adsorbate layer (h=1) is completed. A fraction x of the surface is already covered by h+1 adsorbate layers plus the substrate layer.

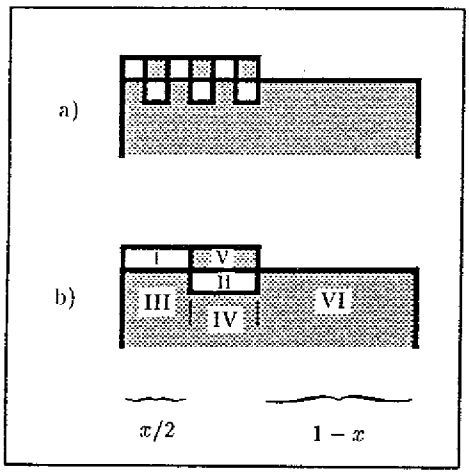

Fig. 7: Alloying of the first deposited ML. (a) is the same as in Fig. 5 b). (b) shows a rearrangement of (a) for reason of simplicity.

The same holds true for the substrate signal, which also gets an additive term for the contribution of the overlayer:

$$I_s = \underbrace{I_{0s}\, x \left(\sum_{i=0}^{\infty} \alpha_s^i\right) \alpha_s^{h+2}}_{\text{III}} + \underbrace{I_{0s}\,(1-x) \left(\sum_{i=0}^{\infty} \alpha_s^i\right) \alpha_s^{h+1}}_{\text{IV}} + \underbrace{I_{0s}}_{\text{V}}$$
$$= I_{0s} \left(1 + \alpha_s^{h+1} \left(\frac{1}{1-\alpha_s} - x\right)\right).$$

Lu[52] observes phenomena of alloying when depositing Pd on Cu(100). An *alloying of the first deposited ML* can be simulated by every second atom (which hits the substrate surface) exchanging its place with the underlying substrate atom (Fig. 5 b). For reason of simplicity all atoms from the second deposited ML on shall grow purely and layer by layer.

Fig. 7 b) shows a situation corresponding to a), but simplified, for $b \leq 1$ ML. In

this case the adsorbate signal is

$$\begin{aligned} I_a &= \underbrace{I_{0a}\,\frac{x}{2}}_{\mathrm{I}} + \underbrace{I_{0a}\,\frac{x}{2}\,\alpha_a}_{\mathrm{II}} \\ &= I_{0a}\frac{x}{2}(1+\alpha_a) \end{aligned}$$

and the substrate signal becomes

$$\begin{aligned} I_s &= \underbrace{I_{0s}\,\frac{x}{2}\left(\sum_{i=0}^{\infty}\alpha_s^i\right)\alpha_s}_{\mathrm{III}} + \underbrace{I_{0s}\,\frac{x}{2}\left(\sum_{i=0}^{\infty}\alpha_s^i\right)\alpha_s^2}_{\mathrm{IV}} + \underbrace{I_{0s}\,\frac{x}{2}}_{\mathrm{V}} + \underbrace{I_{0s}\,(1-x)\sum_{i=0}^{\infty}\alpha_s^i}_{\mathrm{VI}} \\ &= I_{0s}\left(\frac{x}{2} + \frac{1}{1-\alpha_s}\left(\frac{x}{2}\alpha_s + \frac{x}{2}\alpha_s^2 + 1 - x\right)\right). \end{aligned}$$

For the following layer by layer growth, that is $b \geq 1\,\mathrm{ML}$, the parametrization is:

$$\begin{aligned} h &= [b] - 1 \\ x &= b - [b]. \end{aligned}$$

Here we get for the adsorbate signal a product of the signal for $b = 1\,\mathrm{ML}$ and the attenuation by the overlayers as well as two additive terms providing the contributions of the overlayers themselves:

$$\begin{aligned} I_a &= \frac{I_{0a}}{2}\left((1+\alpha_a)\left(x\alpha_a^{h+1} + (1-x)\,\alpha_a^h\right) + x\sum_{i=0}^{h}\alpha_a^i + (1-x)\sum_{i=0}^{h-1}\alpha_a^i\right) \\ &= \frac{I_{0a}}{2}\left((1+\alpha_a)\left(x\alpha_a^{h+1} + (1-x)\,\alpha_a^h\right) + x\,\frac{1-\alpha_a^{h+1}}{1-\alpha_a} + (1-x)\,\frac{1-\alpha_a^h}{1-\alpha_a}\right). \end{aligned}$$

Correspondingly, the substrate signal for $b \geq 1\,\mathrm{ML}$ yields

$$I_s = \frac{I_{0s}}{2}\left(\frac{\alpha_s}{1-\alpha_s} + \frac{\alpha_s^2}{1-\alpha_s} + 1\right)\left(x\alpha_s^{h+1} + (1-x)\,\alpha_s^h\right).$$

Eventually, a *true three-dimensional alloying* can be simulated as shown in Fig. 5 c).

Fig. 8 is a simplification of Fig. 5 c), and with the parametrization

$$\begin{aligned} h &= [b] \\ x &= b - [b] \end{aligned}$$

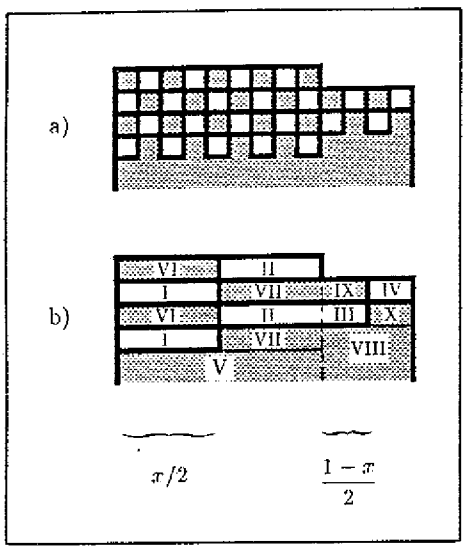

Fig. 8: Three-dimensional alloying. (a) is the same as in Fig. 5 c). (b) shows a rearrangement of (a) for reason of simplicity.

the adsorbate signal can be calculated as

$$
\begin{aligned}
I_a = & \underbrace{I_{0a}\,\frac{x}{2}\left(\sum_{i=0}^{h}\alpha_a^{2i}\right)\alpha_a}_{\text{I}} + \underbrace{I_{0a}\,\frac{x}{2}\sum_{i=0}^{h}\alpha_a^{2i}}_{\text{II}} + \underbrace{I_{0a}\,\frac{1-x}{2}\left(\sum_{i=0}^{h-1}\alpha_a^{2i+1}\right)\alpha_a}_{\text{III}} \\
& \underbrace{+ I_{0a}\,\frac{1-x}{2}\sum_{i=0}^{h-1}\alpha_a^{2i+1}}_{\text{IV}} \\
= & \frac{I_{0a}}{2}\,\frac{1+\alpha_a}{1-\alpha_a^2}\left(x\,(1-\alpha_a^{2(h+1)}) + (1-x)\,(1-\alpha_a^{2h})\right)
\end{aligned}
$$

and the substrate signal as

$$
\begin{aligned}
I_s = & \underbrace{I_{0s}\,x\left(\sum_{i=0}^{\infty}\alpha_s^{i}\right)\alpha_s^{2h+2}}_{\text{V}} + \underbrace{I_{0s}\,\frac{x}{2}\sum_{i=0}^{h}\alpha_s^{2i}}_{\text{VI}} + \underbrace{I_{0s}\,\frac{x}{2}\left(\sum_{i=0}^{h}\alpha_s^{2i}\right)\alpha_s}_{\text{VII}} \\
& \underbrace{+ I_{0s}\,(1-x)\left(\sum_{i=0}^{\infty}\alpha_s^{i}\right)\alpha_s^{2h}}_{\text{VIII}} + \underbrace{I_{0s}\,\frac{1-x}{2}\sum_{i=0}^{h-1}\alpha_s^{2i}}_{\text{IX}} + \underbrace{I_{0s}\,\frac{1-x}{2}\left(\sum_{i=0}^{h-1}\alpha_s^{2i}\right)\alpha_s}_{\text{X}} \\
= & I_{0s}\left[x\left(\frac{\alpha_s^{2(h+1)}}{1-\alpha_s} + \frac{1+\alpha_s}{2}\,\frac{1-\alpha_s^{2(h+1)}}{1-\alpha_s^2}\right) + (1-x)\left(\frac{\alpha_s^{2h}}{1-\alpha_s} + \frac{1+\alpha_s}{2}\,\frac{1-\alpha_s^{2h}}{1-\alpha_s^2}\right)\right].
\end{aligned}
$$

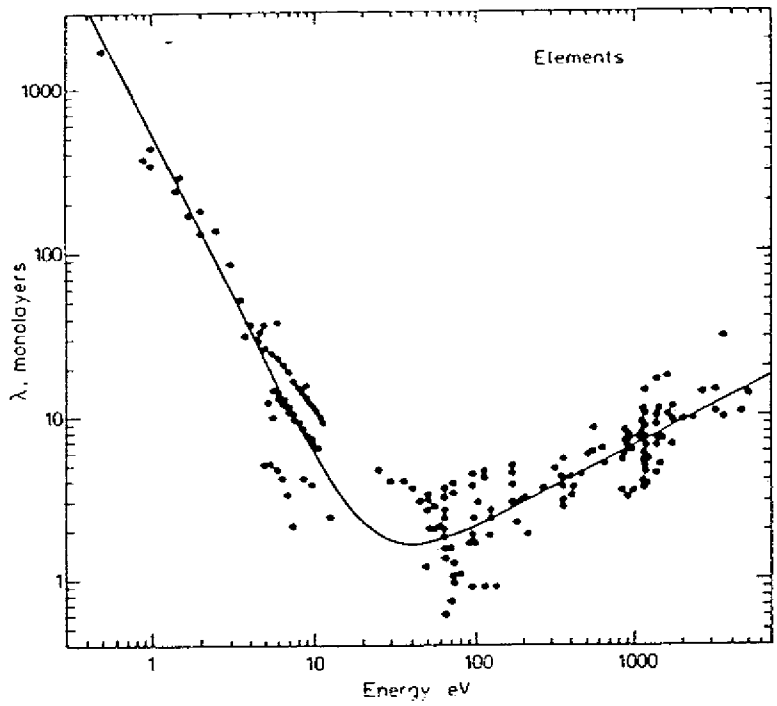

Fig. 9: The dependence of λ on electron energy. (From Ref. 34)

2.2.6. Experimental performance and results

The *universal Seah-Dench equation* (Eq. 2) yields for $E = 330\,\mathrm{eV}$ and a of *bulk* Pd $\lambda_{Pd} = 9.0\,\text{Å}$ and for 650 eV and the same a $\lambda_{Fe} = 12.7\,\text{Å}$. Nevertheless, Fig. 9 shows that the scattering amounts to several ångströms.

An overview Auger spectrum of the clean Fe is displayed in Fig. 10, taken after sputtering, annealing and covering with a thick Fe film.

Clearly visible is the LMM triplet, characteristic of $3d$ transition metals. It consists of the transitions L_3VV (703 eV), $L_3M_{2,3}V$ (651 eV), and $L_3M_{2,3}M_{2,3}$ (598 eV). The sum of all three peak-to-peak heights is taken as the substrate signal.

Fig. 11 is a spectrum after deposition of some 5 ML Pd. Characteristic of Pd are the transitions at 279 eV, 243 eV, and 330 eV, of which the non-resolved duplet $M_{4,5}N_{4,5}N_{4,5}$ (326 and 330 eV) is used as the adsorbate signal.

Two methods have been applied to gain diagrams of Auger intensity versus deposition. Measuring method A is normal incidence and emission of electrons, and it requires to turn the sample after each data point (which is one Auger spectrum) from the analyzer to the evaporator. Method B is continuous evaporation and measurement under angles of 45°. B bears the advantage that the sample does not have to be moved and thus any deviation with reference to the site on the sample

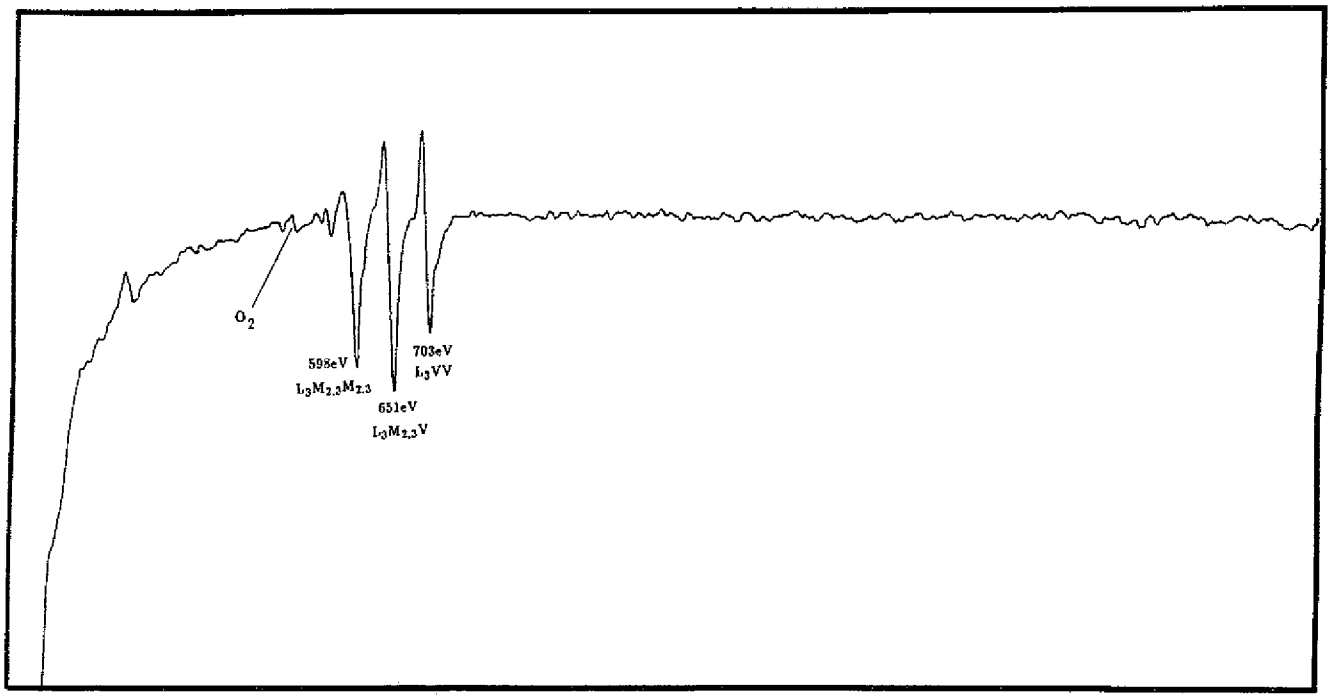

Fig. 10: Overview Auger spectrum of the clean Fe after sputtering, annealing and covering with a thick Fe film. The LMM triplet is characteristic of $3d$ transition metals.

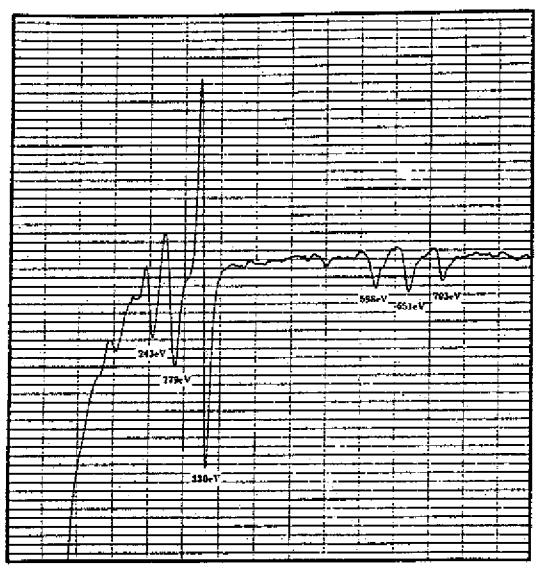

Fig. 11: Auger spectrum of Fe after deposition of about 5 ML Pd.

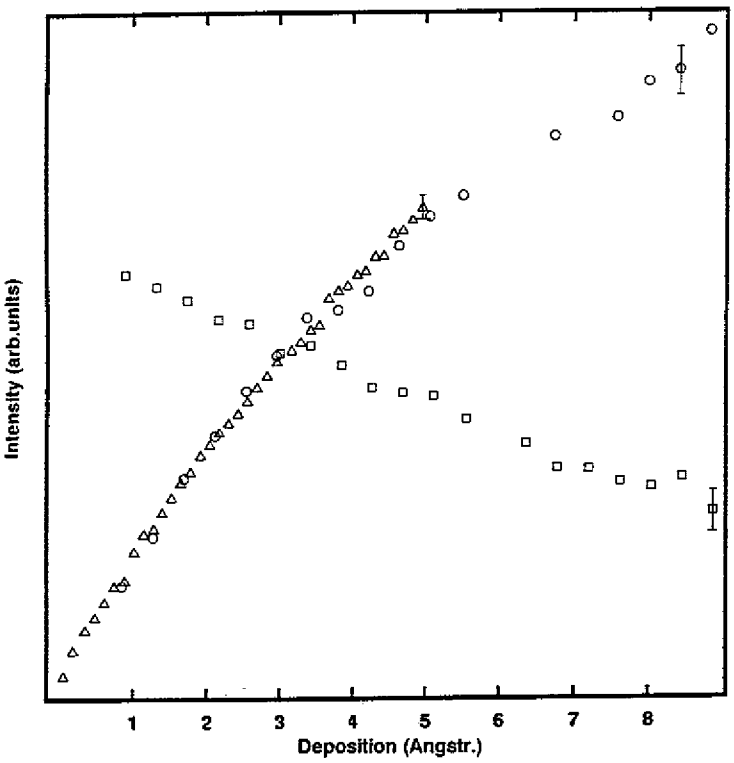

Fig. 12: Auger intensity versus deposited mass for Pd/Fe(100). Fe (squares) and Pd (circles) from zero to 8.8 Å (4.7 ML) thickness according to method A. Pd (triangles) from zero to 5.1 Å (2.7 ML) according to method B. (A and B are explained in the text.)

surface that is probed is ruled out. Yet, the results have to be corrected due to the different geometry.

A quartz crystal microbalance has been used to determine the deposition rate at the site of the sample, this value is the basis for the scale in the diagrams.

First, a measurement according to method A has been performed at a deposition rate of 0.42 Å/min (0.22 ML/min) for the thickness range from zero up to 8.8 Å (4.7 ML) (squares and circles in Fig. 12).

In order to see changes in the slope of the Pd signal, it has been measured with method B at a deposition rate of $(0.34 \cos 45°)$ Å/min = 0.24 Å/min (0.13 ML/min) up to 5.1 Å (2.7 ML) (triangles in Fig. 12).*

In the following the calculated behavior of the Auger signals for the six growth models presented so far will be compared to Fig. 12. As the x-axis is based on the quartz reading, the fit of the theoretical to the experimental curve consists only

---

* In order to compare both measuring methods in the same diagram, two steps were necessary: *(1)* After finishing measurement B an Auger spectrum of the Pd covered sample was taken in normal emission geometry. The data from measurement A were plotted in the form "quotient I_{Pd}/I_{Fe} versus deposition" and by comparing both the total deposition in case B was found to be 2.68 ML. The oscillating quartz yielded in case B a deposition of 2.76 ML, which means agreement within 3%. *(2)* Because of the emission angle of 45° the *inelastic mean free path* λ has to be replaced by the *escape depth* $\lambda \cos 45°$. This was compensated by multiplying the

(as I_{0s} is already determined by the intersection point at the y-axis) in the choice of I_{0a}, which is fitted to the deposition $b = 1\,\mathrm{ML}$. Still, also other possibilities for I_{0a} are taken into account. Furthermore, the model-inherent free parameters will be varied within a physically convenient range. These are the IMFP λ and in case of island growth the covered area divided by the total surface area, denoted x. *Special emphasis is layed on the question whether the experimental data agree with only one or more than one model.*

We first try in Fig. 13 a fit according to *three-dimensional alloying* for $\lambda_a = 6\,\text{Å}$, 9 Å, 12 Å and for $\lambda_s = 5\,\text{Å}$, 10 Å, 15 Å.

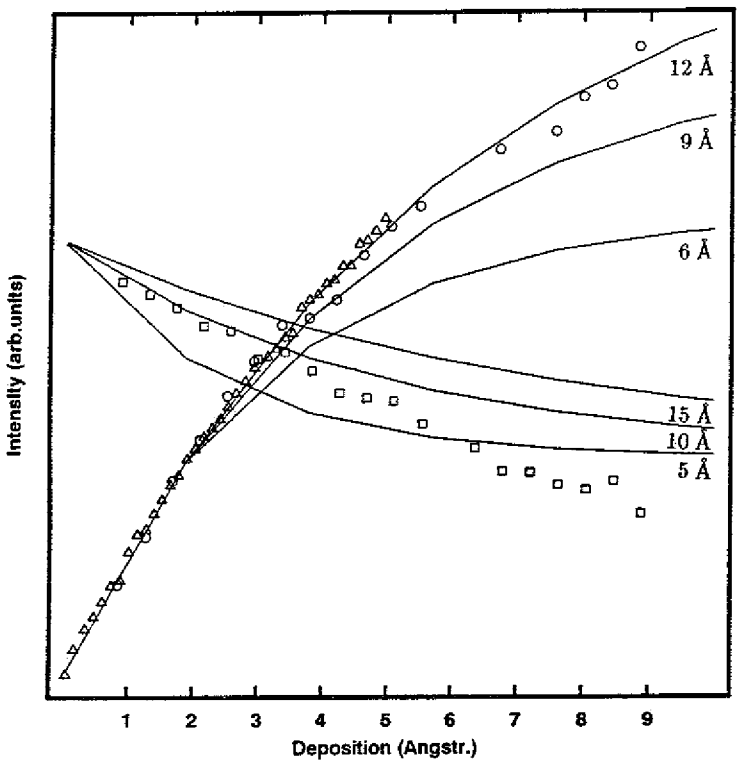

Fig. 13: A fit to the data of Fig. 12 on the basis of the formation of a three-dimensional alloy. The adsorbate signal for λ=12 Å is in agreement with the experimental data whereas the deviation of the substrate signal for λ_s=5 Å, 10 Å, and 15 Å from the measured data shows that in reality the Fe is better screened by the Pd than in a 1 : 1-alloy.

adsorbate signal in B by the corrective factor

$$k = \frac{1 - e^{-\frac{d}{\lambda}}}{1 - e^{-\frac{d}{\lambda \cos 45^\circ}}} \qquad (3)$$

depending on the deposition d. Furthermore no correction had to be made as A and B have been performed at the same modulation amplitude ($4.6\mathrm{V_{pp}}$) and primary electron energy (2.5 keV). [The numerator in Eq. 3 is the envelope of the polygonal shaped adsorbate curve in the *Frank-Van der Merwe* growth. A formula similar to Eq. 3 can be deduced for the substrate.]

The adsorbate signal at an IMFP of 12 Å fits very well to the experimental data, whereas the wide range of λ_s shows that for the substrate no coincidence between model and experiment can be stated. Consequently, in the experiment the Fe is better screened by the Pd than in a 1 : 1-alloy.

Still, an alloy could exist just at the Fe surface and be covered completely by Pd layers. Fig. 14 shows for this model at $\lambda_s = 10$ Å an agreement for the substrate signal, which means high screening and thus good coverage.

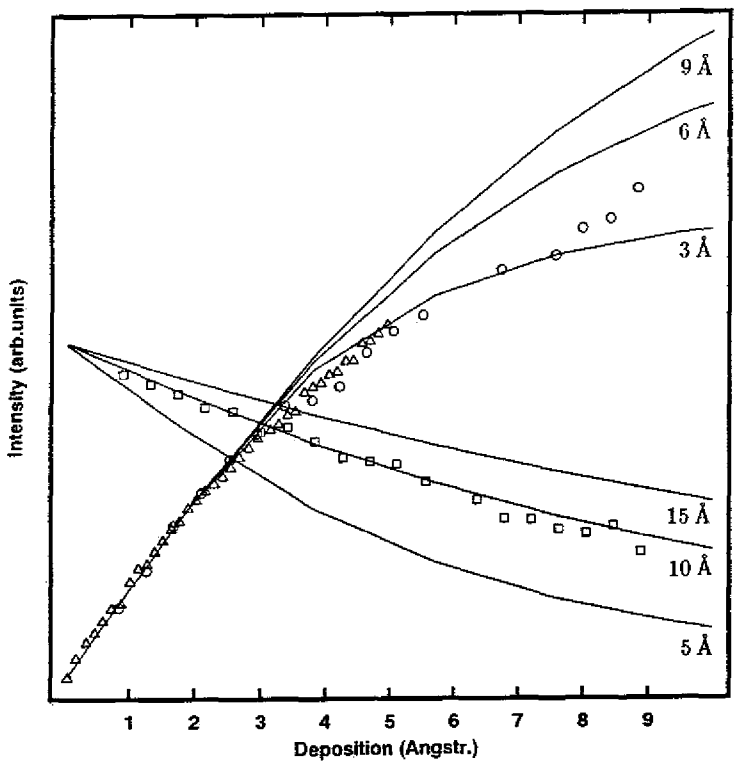

Fig. 14: Comparison of curves for a two-dimensional alloy at the Fe/Pd interface covered by Pd layers with the data of Fig. 12. The theoretical signal of the substrate at λ=10Å shows the same behavior as the measured signal being an indication of a well covered substrate. The theoretical adsorbate signals deviate from the experimental signals because they show nearly no change in their slope between zero and 2 ML.

In contrast, the adsorbate signals differ: the theoretical signal shows nearly no change in its slope between zero and 2 ML. But regarding the experimental curve (triangles) there is a difference in the slope between the first and the second ML. The theoretical curve does not predict any pronounced kink at 1 ML even for an IMFP as low as 3 Å.

As apparent from Fig. 15, an Fe layer permanently situated at the surface leads to a slower attenuation of the Fe signal.

The *Stranski-Krastanov* growth mode shows in general from the second ML on a more slowly increasing adsorbate and decreasing substrate signal. In Fig. 16 $\lambda_a = 6$ Å and $\lambda_s = 10$ Å as well as $x = 0.25$, 0.5 and 0.75 have been chosen, but only in the limit $x \longrightarrow 1$, which corresponds to *Frank-Van der Merwe* growth, the theoretical curves appear to approach the experimental data.

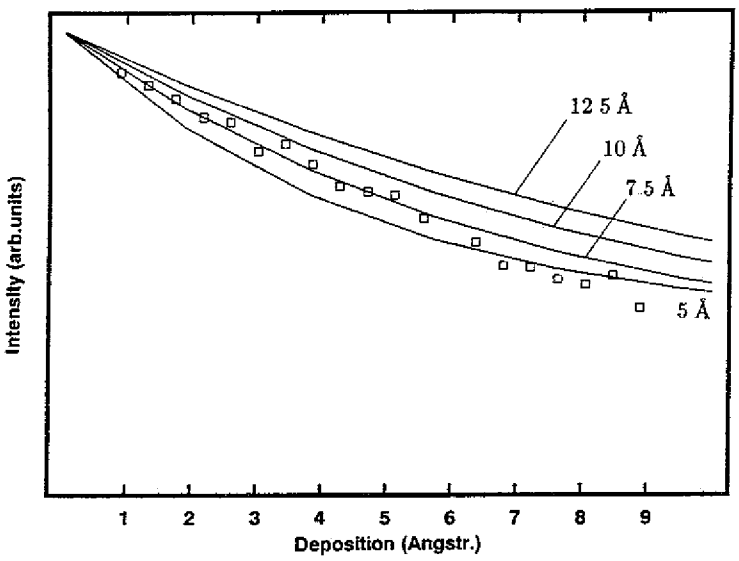

Fig. 15: A monolayer of substrate atoms which is permanently at the surface of the growing adsorbate contributes to the substrate signal and prevents it from decaying. This is not in agreement with the data of Fig. 12.

The plain island growth according to *Volmer* and *Weber* can because of the freedom in choice of I_{0a} lead to unambiguous results only in a comparison of the substrate signals. These are shown in Fig. 17 for three different IMFP, namely 15 Å, 10 Å and 5 Å, and for $x = 0.5$, 0.7 und 0.9. Fig. 17 displays for $\lambda_s = 10$ Å the same increasing coincidence for $x \longrightarrow 1$ as with *Stranski-Krastanov* growth. That this degree of coincidence will not be reached for smaller x and different IMFP, is shown by the curves for $\lambda = 15$ Å with a wrong asymptotic behavior and for $\lambda = 5$ Å with discrepancies at lower deposition.

Eventually, Fig. 18 shows the *Frank-Van der Merwe* growth for $\lambda_a = 6$ Å and $\lambda_s = 10$ Å. This model does not only describe the behavior of the experimental data correctly in principle, but also reproduces the changes in the slope of the adsorbate signal (triangles) at 1 and 2 ML. Generally, in the case of layer by layer growth each adsorbed atom contributes the same to the adsorbate signal, only the factor of proportionality changes from one layer to the next. In addition, the layer by layer growth is the one that produces maximum attenuation of the substrate signal. In order to determine the uncertainty of λ_a and λ_s, in Fig. 19 $\lambda_a = 5$ Å and 7Å and $\lambda_s = 9$ Å and 11Å have been used yielding $\lambda_a = 6 \pm 1$ Åand $\lambda_s = 10 \pm 1$ Å.

In summary, for the system Pd/Fe(100) at room temperature *Frank-Van der Merwe* growth could be established. No indication for interdiffusion was found. An interdiffusion involving about $\frac{1}{5}$ ML Pd would have been recognized by the Auger

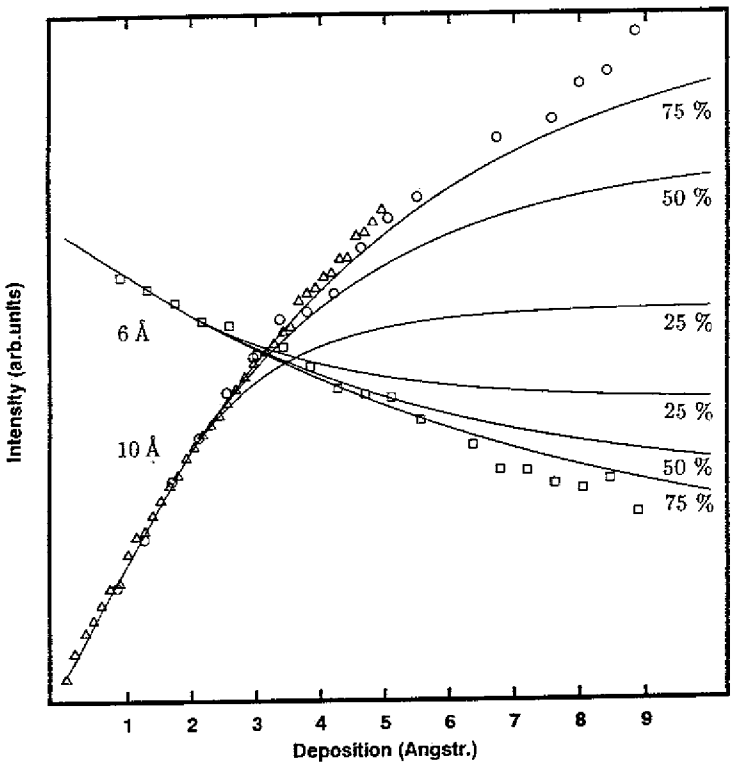

Fig. 16: The *Stranski-Krastanov* growth compared to Fig. 12. Shown are the cases of islands covering 25%, 50%, and 75% of the sample surface after complete monolayer of the adsorbate is deposited. Obviously the agreement between experiment and this growth mode increases with the area covered by the islands.

analysis. The inelastic mean free path of electrons in Pd was found to be 6±1 Å at 330 eV and 10±1 Å at 650 eV.

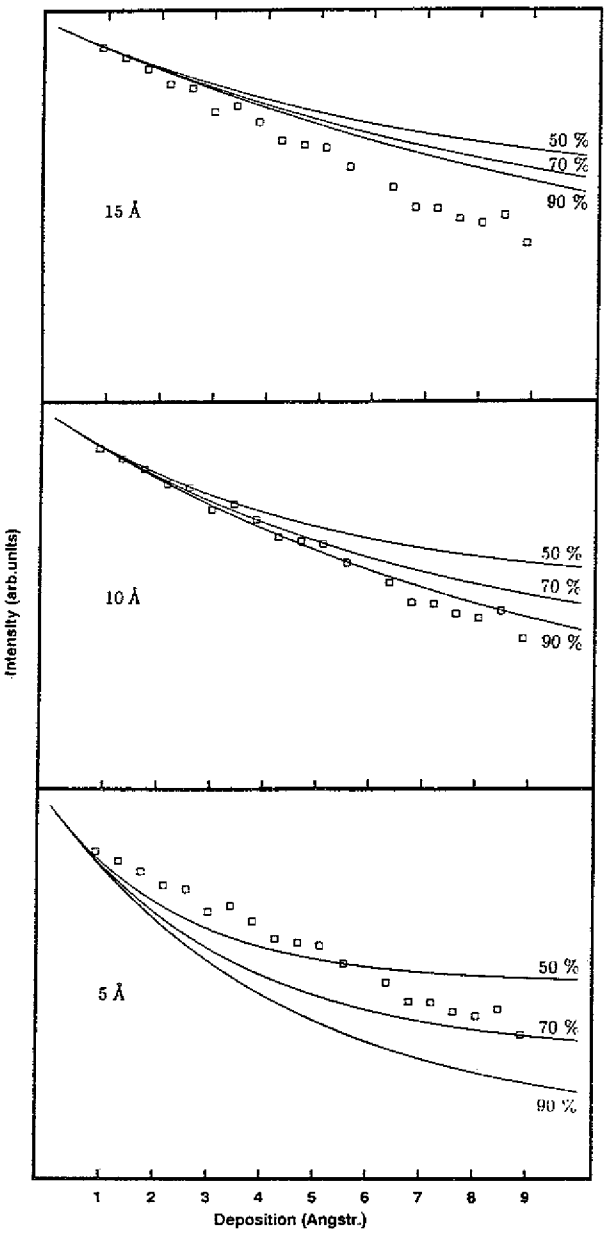

Fig. 17: The substrate signal of Fig. 12 compared to *Volmer-Weber* growth. In this fit two parameters must be varied independently: besides the mean free path λ also the area covered by islands (50%, 70%, and 90% of the surface). None of the plotted curves agrees with the measured data.

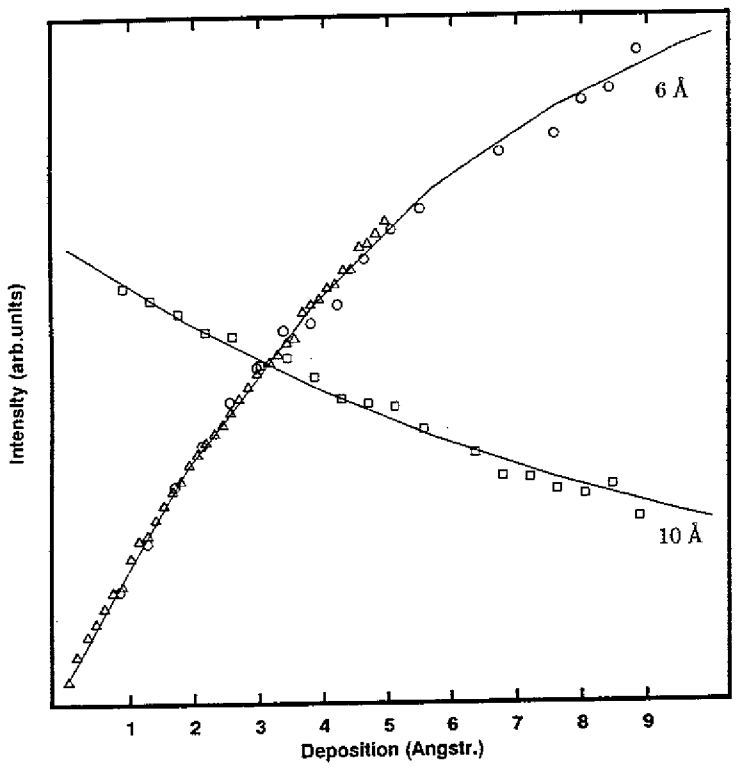

Fig. 18: The *Frank-Van der Merwe* or layer by layer growth mode describes the experimental data of Fig. 12 for for λ_a=6 Å and λ_s=10 Å.

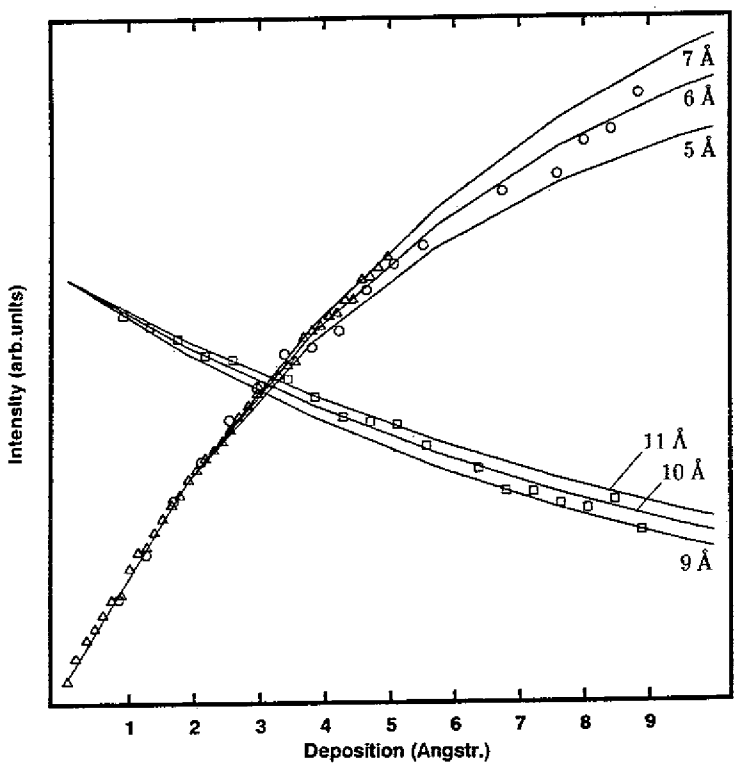

Fig. 19: The inelastic mean free path of electrons in Pd is determined. 6±1 Å at 330 eV and 10±1 Å at 650 eV.

2.3. Application of low-energy electron diffraction

The method of low-energy electron diffraction on crystal surfaces is a strong, although not element specific, tool for studying the atomic structure and degree of order within a surface region of limited depth.

It was in 1921 that *Davisson* and *Kunsman* discovered anisotropies in the angular distribution of electrons backscattered from a metal surface[53]. Not till 1924 when *de Broglie* postulated the wave nature of matter could their results be interpreted on the basis of de Broglie's equation

$$\lambda = \frac{h}{mv}.$$

This was achieved three years later by *Davisson* and *Germer* [54]. The LEED apparatus got its final shape in 1962 when *Lander* constructed a device with spherical grids and a fluorescent screen which enables the view of complete diffraction patterns[55].

In this work the four-grid reverse view LEED system from *Omicron* was used. Its compact electron gun generates monoenergetic electrons of energies up to 1 kV. The outer grids of the analyzer are grounded, the inner grids are connected to a negative potential of about the same magnitude as the accelerating voltage in the electron gun. This potential decelerates the inelastically scattered electrons and thus prevents them from reaching the fluorescent screen.

The formation of the LEED diffraction pattern can easily be understood starting out from a one-dimensional periodic lattice with lattice constant a. Let φ be the incident angle of the electrons with respect to the surface normal. Constructive interference then occurs in the direction ψ if the condition

$$\sin\psi - \sin\varphi = \frac{n\lambda}{a},$$

where n denotes the order of diffraction, is satisfied. Normal incidence and the use of de Brooglie's equation lead to

$$\sin\psi = \frac{n}{a[\text{Å}]}\sqrt{\frac{150.4}{E[\text{eV}]}}$$

where E is the electron energy.

This equation shows that in the case of bcc-Fe with a lattice constant of $a = 2.87\,\text{Å}$ the first order diffraction spots (1,0) appear for the first time at $\psi = 90°$ and $E = 18.2\,\text{eV}$. For $E = 50\,\text{eV}$ the first order spots can be seen at an angle of $\psi = 37°$.* This situation is shown in Table I a) for a sputtered, annealed and

* Such a low energy is desirable since it means a high surface sensitivity.

Fe precovered Fe crystal and $E = 50.2\,\mathrm{eV}$. The sharpness of the spots shows the existence and quality of long range order in the topmost surface layers and their 4-fold symmetry reflects the cubic lattice structure. Concerning the interpretation we are limited to this statement on the *shape* of the unit cell. Further information, i. e. on the *structure* of the unit cell, can be extracted from LEED patterns if one considers the behavior of the intensity of distinct spots with primary electron energy. This is not so much an experimental effort, but an interpretation of the so-called LEED I/V-curves requires comparison with simulated spectra deriving from model calculations.

Nevertheless the conventional LEED analysis is valuable for determining the arrangement of *adsorbate* atoms on a crystal surface. Concerning the three types of two-dimensional rectangular *Bravais* lattices (*square, primitive rectangular*, and *centered rectangular*) the nomenclature distinguishes between p for *primitive* and c for *centered* and denotes the size of the two-dimensional unit cell as the ratios of the lengths of the basis vectors of the adsorbate and substrate lattice (a contribution of the substrate also appears, especially at higher energies, in the LEED pattern) as in *p 1 × 1* or *c 2 × 2*. A possible rotation of the adsorbate lattice with respect to the substrate is expressed by the rotation angle.

Table I b) shows the *p 1 × 1* LEED pattern of the Fe crystal after the deposition of 1ML Pd. There is no difference between the spots in Table I b) and I a) neither in sharpness nor in position. In Table I c) at 2 ML coverage the pattern is still there although the spots loose intensity while incoherently scattered background gains intensity[†]. At a coverage of 3 ML as shown in Table Ig) the pattern is completely lost. In order to study the transition range a new sample was prepared and LEED photographs were taken at 2.3, 2.5, and 2.7 ML which show sharp spots that fade continuously[‡] in the range from 2.3 to 3 ML. As long as the distance of opposing LEED spots can be measured this value shows that no displacement of the spots occurs within 1%. Thus no change in the lattice constant with respect ot the substrate can be attributed to the adsorbate.

Bulk Pd has an fcc-lattice with $a_{Pd} = 3.89$ Å. This fits after rotation by 45° and stretching by $(a_{\mathrm{Fe}}\sqrt{2} - a_{Pd})/a_{Pd} = 4.3\%$ with its (100) surface on top of the (100) face of an Fe bcc lattice with $a_{\mathrm{Fe}} = 2.87$ Å as sketched in Fig. 20.

For the reasons mentioned above fcc and bcc lattices, which exhibit differences only in the stacking of the planes, cannot be distinguished by LEED.

The disappearance of the LEED pattern between 2.7 and 3 ML is due to diminished order of the atomic scatterers. As we have seen in chap. 2.2, the layer by layer growth mode persists at least up to 5 ML. Both results are far from being

---

[†]The LEED photographs I a), b), c), and g) were taken at the same exposure time of 15 s; 10 s for d) and e); 17 s for f); stop-opening always of f 8; screen-voltage 4 kV

[‡]That the lower left spot is hidden in most pictures is due to the electron gun holder.

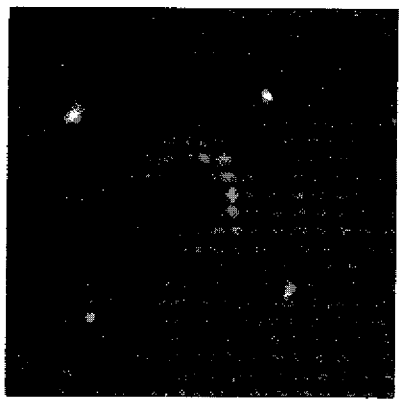

a) Fe

b) 1 ML

c) 2 ML

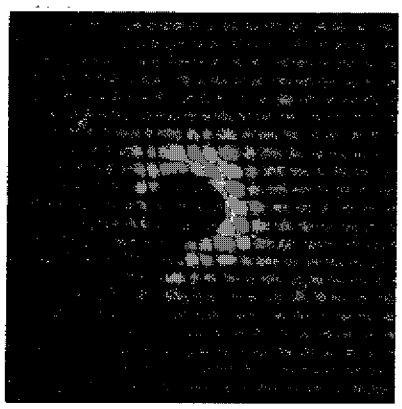

d) 2.3 ML

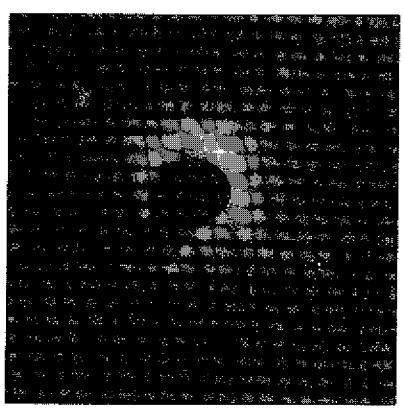

e) 2.5 ML

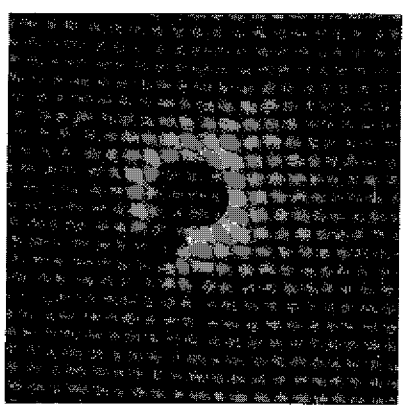

f) 2.7 ML

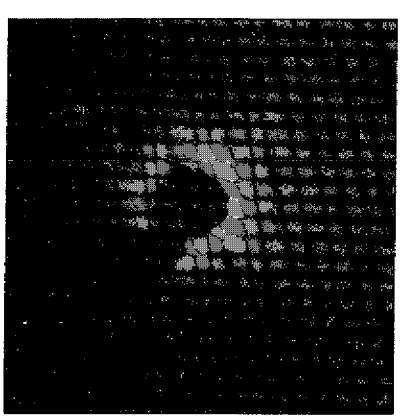

g) 3 ML

TABLE I: LEED PATTERNS OF VARIOUS PD COVERAGES TAKEN AT 50.2 eV PRIMARY ELECTRON ENERGY

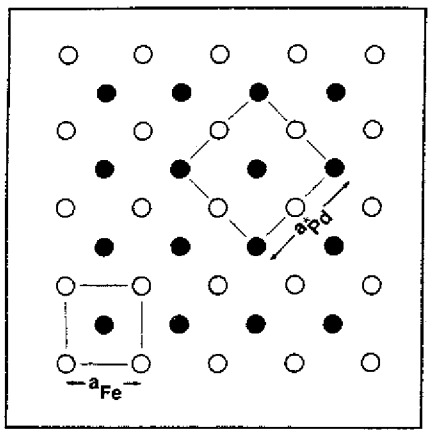

Fig. 20: Growth of Pd on bcc Fe(100). Fe atoms (○) of the topmost (s) layer of the bcc Fe(100) surface and Pd atoms (●) forming the first adsorbate layer (s+1). In plan view fcc and bcc are cannot be distinguished.

in contradiction as on the one hand LEED, operated at lowest kinetic energies, probes predominantly the structure of the *topmost* surface layer and AES, on the other hand, tells us in this case that one layer is accomplished before the next one is begun and does not tell us if and to what extent long-range order *within* the layers is fulfilled. The reason for the disappearance of long-range order within the topmost layer can be for instance that the arrangement of Pd atoms "switches" to e. g. the Pd bulk lattice constant within areas whose extent is less than the LEED coherence width of 50 to 100 Å and which are not ordered with respect to each other. An investigation of the in-plane atomic arrangement in this stage of growth must be left to future STM studies.

3. Photoelectron spectroscopy — general aspects

3.1. Phenomenology

In angle-resolved photoelectron spectroscopy the surface of a sample is irradiated by monochromatized light of enery $h\nu$ and the consequently emitted electrons are analyzed with respect to direction (θ, φ, cf. Fig. 21) and kinetic energy E_{kin}.

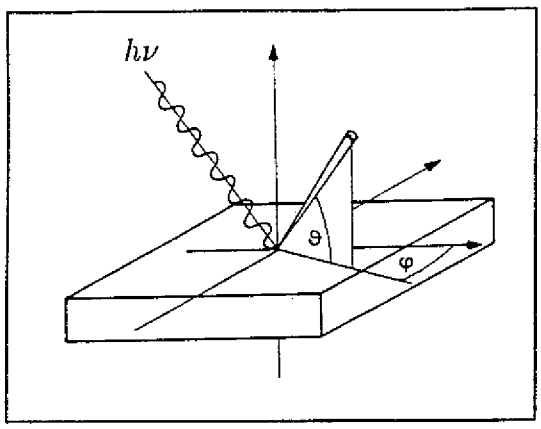

Fig. 21: Photoemission geometry

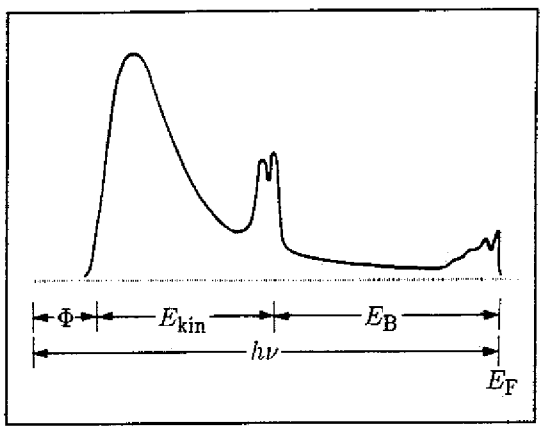

Fig. 22: Schematically drawn photoelectron spectrum

Fig. 22 shows a typical photoelectron spectrum and the energy relationships that are basical for its understanding. The more than all employed relationship is *Einstein*'s equation

$$E_{\mathrm{kin,max}} = \hbar\omega - \Phi \tag{4}$$

published[56] in 1905 saying that the maximum kinetic energy of an electron emitted in the photoelectric effect is equal to a quantized photon energy minus the energy (work function) necessary to release the electron from the solid. On the right hand side of Fig. 22 the electrons of highest kinetic energy, which correspond to the most loosely bound electrons, are found — namely those deriving from the Fermi edge. In order to extend Eq. 4 also to the other electrons in the spectrum the *binding energy* is defined by

$$E_B = \hbar\omega - E_{\mathrm{kin}} - \Phi. \tag{5}$$

Electrons deriving from the *valence band* can be found at binding energies of several eV while those from *core levels* contribute between several ten eV and several ten thousand eV. Besides other features in the spectrum like Auger peaks and satellites the background of inelastically scattered electrons appears increasing with E_B up to the edge of electrons of zero kinetic energy.

3.2. Theory of photoemission

In photoemission models, especially if one wishes to go beyond the explanation of the energy position E_B of spectral features towards considering *intensities*, photoemission of an electron has to be treated in the framework of quantum mechanics as a transition from an occupied eigenstate (the initial state $|\psi_i>$) to the final state $|\psi_f>$ of a quantum mechanical system*. The transition rate between two eigenfunctions of the Hamiltonian H' is given by Fermi's golden rule

$$P_{fi} = \frac{2\pi}{\hbar} \left| <\psi_f | H' | \psi_i> \right|^2 \delta(E_f - E_i - \hbar\omega) \tag{6}$$

where the δ distribution guarantees conservation of energy and H' denotes the Hamiltonian for the interaction between an electron and a vector potential of the electromagnetic radiation field $\mathbf{A}$ neglecting higher order contributions (dipole approximation):

$$H' = \frac{e}{2mc} \mathbf{A} \cdot \mathbf{p}$$

Here $\mathbf{A}$ is assumed to be constant and fixed in space, so that[57]

$$P_{fi} \propto \left| <\psi_f | \mathbf{p} | \psi_i> \mathbf{A} \right|^2 \delta(E_f - E_i - \hbar\omega). \tag{7}$$

Applying the commutation relationship[58] of $H = p^2/2m + V(\mathbf{r})$ with $\mathbf{p}$ and $\mathbf{r}$

$$<\psi_f | [\mathbf{p}, H] | \psi_i> = (E_i - E_f) <\psi_f | \mathbf{p} | \psi_i> = -ih <\psi_f | \nabla V | \psi_i>$$
$$<\psi_f | [\mathbf{r}, H] | \psi_i> = (E_i - E_f) <\psi_f | \mathbf{r} | \psi_i> = \frac{ih}{m} <\psi_f | \mathbf{p} | \psi_i>$$

and with the equation $\hbar\omega = E_f - E_i$ one gets two different forms of the matrix element in Eq. 7:

$$<\psi_f | \mathbf{p} | \psi_i> = im\omega <\psi_f | \mathbf{r} | \psi_i> = \frac{i}{\omega} <\psi_f | \nabla V | \psi_i>$$

Here the last expression specifies a requirement for photoemission models by showing that photoemission cannot take place in a potential $V(\mathbf{r}) = \text{const.}$

The simplest case in which photoemission occurs is a free-electron system bound by a potential barrier located at the site of the two-dimensional interface between the semi-infinite solid and vacuum. With $\mathbf{e}_z$ as the unit vector normal to the surface one gets

$$\nabla V = \frac{\partial V}{\partial z} \mathbf{e}_z$$

*What is included in the system will be defined later.

and Eq. 7 simplifies to

$$P_{fi} \propto \left| <\psi_f | \frac{\partial V}{\partial z} | \psi_i > A_z \right|^2 \delta(E_f - E_i - \hbar\omega).$$

If we attribute single-crystal properties to the solid, then V becomes a periodic potential and the states ψ_i and ψ_f satisfy the Bloch condition

$$\psi(\mathbf{r} + \mathbf{q}) = e^{i\mathbf{k}_{\|}\cdot\mathbf{q}} \psi(\mathbf{r}) \tag{8}$$

as a consequence of the translational symmetry parallel to the surface ($\mathbf{q}$ denotes a lattice vector in that surface). For the wave vector $\mathbf{k}$ of the electron Eq. 8 results in the conservation[59] of its component parallel to the surface $\mathbf{k}_{\|}$ on the passage through the two-dimensional surface barrier, but plus or minus a reciprocal surface lattice vector $\mathbf{G}$:

$$\begin{aligned} \mathbf{k} &= \mathbf{k}_{\|} + \mathbf{k}_{\perp} \\ \mathbf{k}_{i\|} &= \mathbf{k}_{f\|} \pm \mathbf{G} \end{aligned} \tag{9}$$

Thus $\mathbf{k}_{i\|}$ is known in the reduced Brillouin zone if the wave vector outside of the solid $\mathbf{k}^{\text{ext}}$ which we identify with $\mathbf{k}_f$ can be determined. As the electron having left the solid is a free electron its wave vector satisfies

$$|\mathbf{k}^{\text{ext}}| = \sqrt{\frac{2m}{\hbar^2} E_{\text{kin}}}$$

and we get its parallel component from

$$\mathbf{k}_{\|}^{\text{ext}} = \sqrt{\frac{2m}{\hbar^2} E_{\text{kin}}} \sin\theta \tag{10}$$

$$\mathbf{k}_{\perp}^{\text{int}} = \sqrt{\frac{2m}{\hbar^2} E_{\text{kin}}} \cos\theta. \tag{11}$$

More complicated is the question for $\mathbf{k}_{i\perp}$. From the theoretical point of view the answer depends on what we mean with the "system" described by Eq. 6. Historically the first model of photoemission that was able to predict *intensities* correctly was the *three-step model*[60,61,62,63] published to my knowledge in its most elaborate form by *Berglund* and *Spicer* [64] in 1964. The *first step* is the creation of a photoelectron within the solid, the *second step* describes the transport of the electron to the surface of the solid and allows scattering effects. In the *third step* the electron eventually leaves the solid.

The first step is treated quantum mechanically by evaluating the matrix element from Eq. 6. Thus the final state $|\psi_f>$ lies within the solid and is a bulk

property. Thus the influece of the surface on the excitation of the photoelectron, e. g. excitation from or into a surface state[67,68], is ruled out in the model.

The transition is depicted in the band structure by a *direct* transition from an occupied initial state below to an unoccupied final state above the Fermi edge with the energy difference between both determined by the photon energy as

$$E_f(\mathbf{k}^{\text{int}}) - E_i(\mathbf{k}^{\text{int}}) = \hbar\omega. \tag{12}$$

Note that characterizing the transition as "direct" or "optical" implies that $\mathbf{k}_\parallel$ as well as $\mathbf{k}_\perp$ are conserved during the first step. The second step had to be calculated independently from step one by introducing a *mean free path* λ of the electron in the solid. A consequence also not considered in the model is the influence of λ on the conservation of $\mathbf{k}_\perp$ on the way of the electron to the surface. If λ, which we will identify with the IMFP from chap. 2.2, is much greater than the interplanar spacing the coherence of excitations from different layers leads to a conservation of $\mathbf{k}_\perp$. If, on the other hand, λ is of the same order of magnitude or less than the interplanar distance also transitions that do not conserve $\mathbf{k}_\perp$ exactly are allowed, and a broadening[65,*] of $\mathbf{k}_{f\perp}$ sets in.

In a *one-step model*[73] the whole excitation starting from the initial state within the solid until the final state, which is located in the detector, is a single quantum mechanical transition. The question which arises is: What is the nature of the final state that has to be inserted in the matrix element of Eq. 6?

The electron is — apart from inelastic scattering which determines the IMFP — also affected by elastic scattering which changes its angular distribution. Backscattering leads for instance to large gaps in the final state band structure, e. g. found in normal emission from Cu (100).[74,†] *Mahan* [75] introduced these scattering effects into photoemission when he identified $|\psi_f>$ with a *time reversed LEED state*, which means a plane wave starting from the detector, but time reversed as we deal with *emission*. *Liebsch* established a one-step model of photoemission on the basis of time reversed LEED states[69], and showed that it is especially suitable for the treatment of overlayers[70,71] and layer compounds[72]. The IMFP which causes the reduced probing depth in photoemission is included by means of an *optical potential* which renders $\mathbf{k}_\perp$ complex.[58]

However, the by far simplest approach to the final state is suggesting a free electron final state inside of the crystal and describing the ionic potential of the

---

*By inserting values typical of metals (a mean free path λ=4Å and an interplanar spacing of 2Å) into Heisenberg's uncertainty principle *Thiry* (Ref. 66) finds for $\Delta\mathbf{k}_\perp$ 20% of the size of the Brillouin zone.

† If bulk final states are not accessible at a certain photon energy, the surface sensitivity of the experiment will be enhanced.

solid by an average V_0 providing

$$E_f = \frac{\hbar^2}{2m}\left(\mathbf{k}_{f\parallel}^2 + \left(\mathbf{k}_{f\perp}^{\mathrm{ext}}\right)^2\right)$$

$$E_f + V_0 = \frac{\hbar^2}{2m}\left(\mathbf{k}_{f\parallel}^2 + \left(\mathbf{k}_{f\perp}^{\mathrm{int}}\right)^2\right)$$

and thus

$$\mathbf{k}_{f\perp}^{\mathrm{int}} = \sqrt{\left(\mathbf{k}_{f\perp}^{\mathrm{ext}}\right)^2 + \frac{2mV_0}{\hbar^2}}. \tag{13}$$

V_0 can either be regarded as an adjustable parameter in a band mapping experiment (which consists to a considerable extent of comparison of experimental with calculated data) or it can be taken as a value provided by theory, approximately as the zero of the muffin tin potential in an augmented plane wave band structure calculation.[66]

3.3. Symmetries and selection rules

Band mapping experiments whether they aim at gaining a two-dimensional band structure of surfaces and overlayers from the variation of $\mathbf{k}_{\parallel}$ or a three-dimensional bulk band structure by varying $\mathbf{k}_{\perp}$ derive great benefit from a symmetry argument. Furthermore selection rules are advantagous for any photoemission experiment where a source of polarized light (synchrotron radiation) is available and the symmetry properties of the crystalline sample as well as those of the light are known. For a proper description of the experimental conditions a few definitions are needed:

(1) Reflection about a *mirror plane* will transfer the crystal lattice into itself. Mirror planes of a semi-infinite crystal or a crystal film must obviously be perpendicular to the surface plane. In the case of cubic lattices with (100) surface there are four mirror planes, namely (010), (001), (011) and $(0\bar{1}1)$.

(2) Let the plane defined by the propagation vector of the irradiating light and the detection direction be called *detection plane.*

(3) Linear polarization of light, characterized by a polarization direction (the direction of the vector potential **A** perpendicular to the propagation vector) that is fixed in space, can either be *s-polarization* or *p-polarization. s*-polarized light means that **A** lies in the crystal surface, this can be for instance achieved by normal incidence; *p*-polarized light requires a polarization vector **A** perpendicular to the surface, which can only be achieved by off-normal incidence. That is why at most *predominantly p-polarized* light is (by grazing incidence) attainable (Fig. 23).

In mirror plane emission no final state of odd parity with respect to reflection about the mirror plane is possible.[76] The reason is that as a continuous function

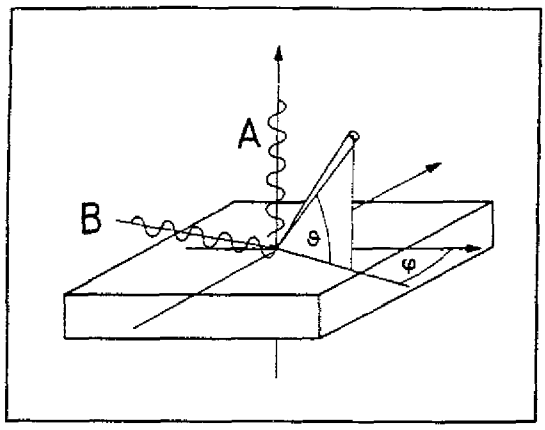

Fig. 23: s-polarized light (A); predominantly p-polarized light (B).

an odd final state ψ_f has to have a point of zero in the mirror plane. With this knowledge of the final-state symmetry and the polarization of the light one can determine the initial-state symmetry from Tab. 1 taken from Ref. 76.

Crystal	Coordinate Axes			Irreducible	Initial State Symmetry		
Face	x	y	z	Representations	A ∥ x	A ∥ y	A ∥ z
(001)	[100]	[010]	[001]	$\Delta_1\ \Delta_1'\ \Delta_2\ \Delta_2'\ \Delta_5$	Δ_5	Δ_5	Δ_1
(110)	[001]	[1$\bar{1}$0]	[110]	$\Sigma_1\ \Sigma_2\ \Sigma_3\ \Sigma_4$	Σ_3	Σ_4	Σ_1
(111)	[$\bar{1}$10]	[$\bar{1}\bar{1}$2]	[111]	$\Lambda_1\ \Lambda_2\ \Lambda_3$	Λ_3	Λ_3	Λ_1

Tab. 1: Dipole-allowed initial state symmetries for normal emission from cubic faces. With the z-axis in the direction of the surface normal the cases $\mathbf{A}\|x$ and $\mathbf{A}\|y$ correspond to s-polarized light, $\mathbf{A}\|z$ corresponds to p-polarization. (Table from Ref. 76. Similar tables for the more general case of off-normal emission can be found in Ref. 77.)

3.4. The technique of angle-resolved photoelectron spectroscopy

In his pioneering photoelectron spectroscopy experiments, or *electron spectroscopy for chemical analysis (ESCA)* as he called it, *Siegbahn*[78] started with magnetic fields as the dispersive element of his spectrometer. *Turner*[79] used a retarding field analyzer for his ultraviolet photoelectron spectroscopy (UPS) work. Nowadays in most of all cases electrostatic analyzers are used. They consist of two capacitor plates held at different potentials. An electron that passes through the electric field will be deflected, and if its path is fixed by means of apertures one can choose the

energy of the transmitted electrons — the *pass energy* — by varying the voltage of the capacitor plates. Cylindical or spherical shape of the plates increases the resolution as a consequence of their focussing properties. A review of electrostatic analyzers can be found in Ref. 80. Important is the fact, that the dependence of the pass energy on the applied voltage is linear and a whole spectrum can be taken easily by applying a ramp voltage to the analyzer.

In this work a 90°-spherical analyzer with an energy resolution of about 250 meV at an angular acceptance of ±3° has been used. The analyzer, which is schematically shown in Fig. 24, is similar to the one described by *Gudat et al.*[81] and *Kisker et al.*[82].

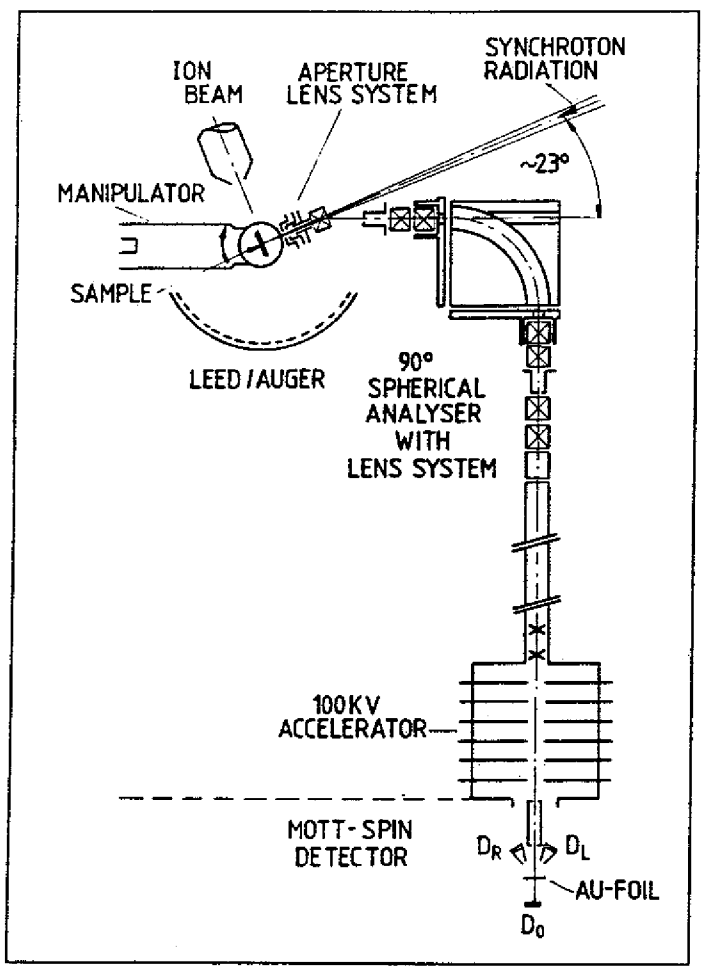

Fig. 24: Scheme of the analyzer. The manipulator allows different emission geometries; an entrance lense system determines the solid angle of detection and thus enables angular resolution; a pair of capacitor plates deflects the electrons into the 90° analyzer spheres; an accelerator followed by a Mott spin detector is aligned to the exit of the analyzer.

The difference consists mainly in the way in which in normal emission normal-incidenting (thus *s*-polarized) light, i. e. coincidence of the collection direction of the detector and the propagation direction of the light, is realized. In the apparatus of Ref. 81 and Ref. 82 this was achieved by a plane mirror near the axis of

the electron optics. In the apparatus used in this work normal incidenting (thus s-polarized) light at normal collection direction is realized by a pair of capacitor plates which deflect the electrons from the light axis. *Off-normal* collection directions can be reached by tilting the sample. If the sample is turned around an axis parallel to the polarization vector, s-polarization will be preserved, otherwise s- and p-polarization will mix up.

3.5. Principles and technique of spin-resolved photoelectron spectroscopy

Up to this time we have considered the measurement of three initial state properties of the electron, as there are that of the binding energy by determining the kinetic energy, that of $\mathbf{k}_{\parallel}$ by choosing the angle of detection and measuring the kinetic energy and that of $\mathbf{k}_{\perp}$ also by evaluating angle and kinetic energy and assuming a final state. Now we will concentrate on the *spin* of the electron.

The observable in a spin-resolved photoemission experiment is the *electron spin polarization* P which is defined[86] as the expectation value of the Pauli spin operator σ:

$$P = <\sigma> = \mathrm{Trace}(\sigma\rho)$$

The spin polarization with respect to a certain direction, the quantization axis which is provided by the experimental set-up as will be pointed out below, becomes

$$P = \frac{N^{\uparrow} - N^{\downarrow}}{N^{\uparrow} + N^{\downarrow}} \tag{14}$$

where $N^{\uparrow}$ and $N^{\downarrow}$ are the numbers of electrons with magnetic moments parallel to the given quantization axis and antiparallel respectively.

P is measured in most cases by means of *Mott scattering*. *Mott* [87] discovered in 1929 that the spin dependent terms in the Coulomb scattering from heavy atoms arise from relativistic L-S coupling and cause a left-right intensity asymmetry A. In the apparatus used in this work the photoelectrons are accelerated after having left the energy analyzer to about 100 keV and scattered from a thin Au foil target (Fig. 24). Two Si surface barrier detectors* placed symmetrically at scattering angles of $\pm 120°$ measure the intensities N_1 and N_2 respectively. The asymmetry A is defined as

$$A = \frac{N_1 - N_2}{N_1 + N_2}.$$

---

* A third Si detector is placed behind the Au foil and measures conventional angle-resolved photoemission spectra, from now on referred to as *spin-integrated* spectra.

A is related to the polarization P in the axis perpendicular to that defined by both detectors. In our case the former is the vertical, so that in normal emission geometry the in-plane magnetization is probed. A depends on P like[88]

$$A(P) = \frac{A_a + PS}{1 + A_a PS}$$

where S denotes the *Sherman function* which measures the "efficiency" of the spin analyzer and has a maximum[89] for 100 keV electrons at a scattering angle of 120°. Because of multiple scattering S decreases with the thickness of the scattering foil. In this case of a Au foil of about 300 Å thickness holds $S \approx 0.2$. A_a is the *apparatus asymmetry* which is canceled out to a large extent by reversing the magnetization of the sample[90] and taking for P the average of the measured asymmetries of both magnetization directions $\bar{A}$ devided by the Sherman function:

$$P = \overline{A}/S$$

With the known (spin-integrated) spectrum $I_0(E_B)$ and the known polarization curve $P(E_B)$ one gets the spin-resolved spectra $I^{\uparrow}(E_B)$ and $I^{\downarrow}(E_B)$ from

$$I^{\uparrow}(E_B) = \frac{1}{2} I_0(E_B)\,(1 + P(E_B))$$
$$I^{\downarrow}(E_B) = \frac{1}{2} I_0(E_B)\,(1 - P(E_B)).$$

As for ferromagnets the number of photoelectrons with their magnetic moments* aligned parallel to the magnetization direction predominates $I^{\uparrow}(E_B)$ is called *majority spin* spectrum and $I^{\downarrow}(E_B)$ *minority spin* spectrum. The essence of the preceeding chapter can be found summarized in Tab. 2.

Initial State Property	Corresponding Observable Parameter	Mediating Equation
binding energy	kinetic energy	5
$\mathbf{k}_{\parallel}$	kinetic energy, detection angle	9, 10
$\mathbf{k}_{\perp}$	kinetic energy, detection angle	11, 13
spin	polarization	14

Tab. 2: The initial state properties probed in a photoemission experiment, parameters actually measured, and the equations combining both.

* Note that for electrons spin and magnetic moment are antiparallel.

Spin-resolved photoemission requires that the way of the photoelectron from the sample to the (electrostatic) energy analyzer is free of magnetic fields which would lead to a precessional motion of the electron spin around the field direction and cause a loss of spin information. But the light spot focused on the sample as well as the solid angle of the detector determine a macroscopic probing area of typically 0.5 mm in diameter on the sample surface. This exceeds by far the size of the Weiss domains of an unmagnetized sample. This means that in order to prevent a mixing in the spin information of the photoemitted electron beam the sample has to be remanently magnetized prior to photoemission in order to render it one single domain. Two sample geometries are known[83] that can be remanently magnetized *in-plane* and exhibit only a negligible magnetic stray field, as there are a thin film (on top of a dia- or paramagnetic substrate) and a picture frame shaped bulk crystal. For the *picture frame crystal* — cut with regard to the magnetic easy axis and magnetized by a coil wrapped around one leg as displayed in Fig. 25 — there are predominantly four domains and the lines of force stay within the solid.

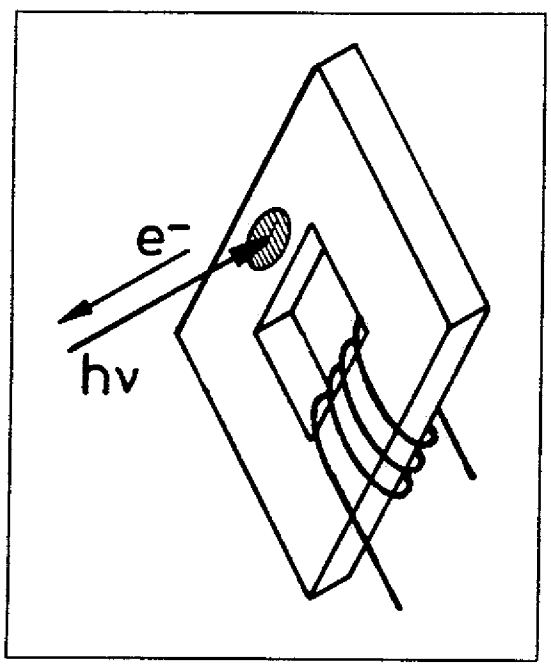

Fig. 25: Picture frame crystal with magnetization coil. The shaded area marks the surface region probed in an angle-resolved photoemission experiment.

Regarding possible effects within the solid the question for a "spin-dependent scattering" of the photoelectron when crossing a magnetic layer on its way to the sample surface has been raised[84] and is still under discussion[85]. In this work a "spin filter effect" is not expected as the kinetic energies are $\geq$ 15 eV and apart from that the overlayer is the less magnetic material.

4. Photoelectron spectroscopy — experimental results

4.1. Spin-integrated photoelectron spectroscopy

4.1.1. Selection of the photon energy

For the spin- and angle-resolved spectra a photon energy of $h\nu = 21\,\mathrm{eV}$ has been chosen for the following reasons:

(1) At 21 eV the photoionization cross section for the Pd 4*d* subshell is close to its maximum, which is found at about 30 eV[93]. The tabulated cross sections[93] reveal a Pd 4*d* value at 21.2 eV that is 5.4 times larger* than that for the Fe 3*d* subshell. This fact is very important as it allows spectroscopy in the monolayer and submonolayer regime.

(2) The widespread use of He I radiation for UPS studies in times before storage rings became a common light source has produced a huge amount of spin-integrated reference spectra at 21.2 eV, this is also the case with Pd[94,95,96].

4.1.2. Pd coverage dependence

Onto the sputtered, annealed, and Fe-precovered Fe sample Pd atoms have been evaporated amounting to 0.2±0.05 up to 4±0.5 ML and the evolution of the valence band has been monitored in spin-integrated photoemission spectra at 21 eV photon energy. During the evaporation as well as during all photoemission measurements the sample was held at room temperature.

Although spin-resolved data will later reveal that the formation of the Pd electronic structure starting out from randomly spreaded atoms of the early submonolayer regime *via* the monolayer and bilayer towards the bulk exhibits considerable differences with respect to majority and minority spin contributions, already from the spin-integrated spectra of Fig. 26 several features can be extracted:

(1) The Pd-derived structure in the spectra starts to grow at about 2.6 eV binding energy as seen from the 0.2 ML spectrum, whereas the center of gravity of the peak dominant in the *monolayer* spectrum is located at about 2 eV. The 0.4 ML spectrum shows an intermediate stage of this shift by locating the Pd structure at 2.4 eV. That the shift is not due to a simple superposition of Pd and the Fe structure at about 2.6 eV binding energy can be seen from subtractions (not shown) of the clean Fe spectrum from the 0.2 and 0.4 ML Pd spectra and will also become clear from spin-resolved spectra later.

(2) Pd and Fe contributions to the valence band spectra are strongly overlapping and cannot, especially from the 1.6 ML spectrum on, be separated easily. The

* Although the tabulated absolute values hold for the *atom*, the ratio between the Pd and the Fe values is not expected to differ much in the bulk case.

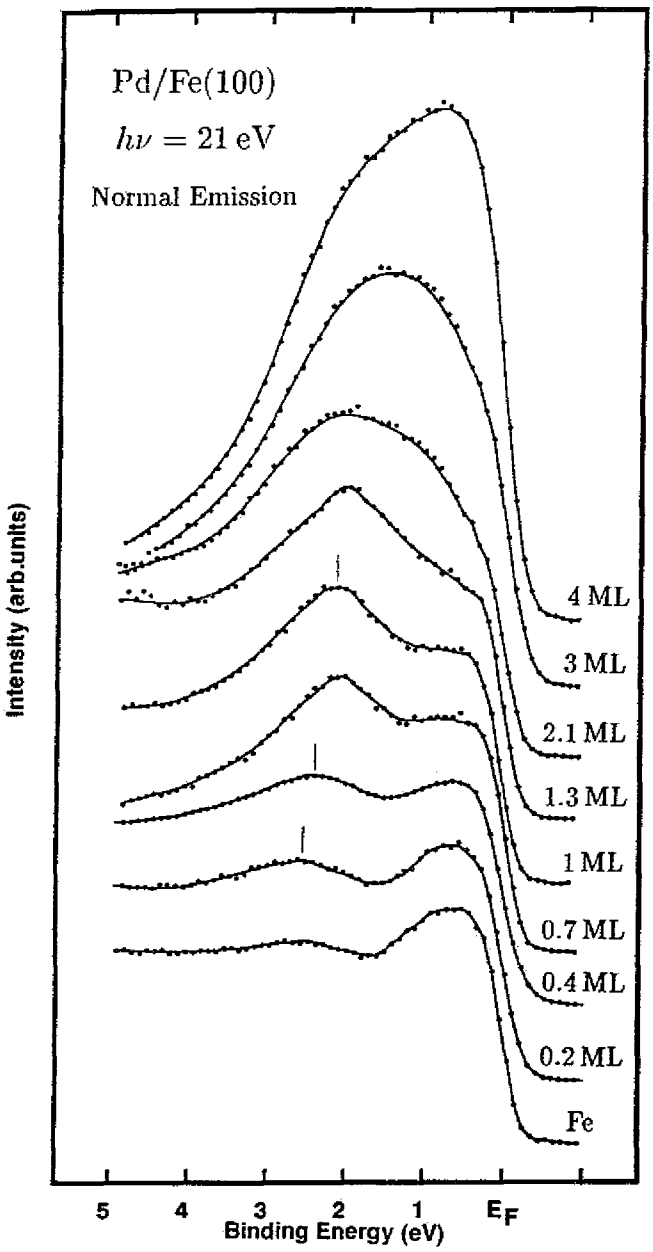

Fig. 26: Spin-integrated valence band spectra at $h\nu$=21 eV, s-polarization, and normal emission from clean Fe(100) and Pd coverages of 0.2±0.05, 0.4±0.1, 1±0.1, 1.3±0.1, $2.1^{+0.2}_{-0.1}$, 3±0.5, and 4±0.5 ML.

difference in the photoionization cross section between Fe and Pd at $h\nu = 21$ eV proves to be helpful in this situation as our concern are mainly the properties of the Pd overlayer.

(3) Bulk Pd is found at 4±0.5 ML coverage and verified by successive Pd deposition without any noticible change in the spectrum. It shows a shoulder at about 2 eV corresponding to the relatively sharp monolayer feature at the same binding

energy, and exhibits its predominant intensity close to the Fermi edge. A comparison with published HeI spectra from Pd single crystals in normal emission geometry and with 20° [94] and 15° [95] incident photons shows that the emission from Pd(100) does not occur essentially near E_F. Pd(110) spectra[94,96] have a shape more similar to the spectrum taken from 4 ML Pd/Fe(100). This is not surprising considering the disappearance of the LEED pattern in the coverage regime of 3 ML, which indicates a rearrangement of the surface layer as pointed out above. On the other hand, the Pd(111) spectra[94] with their double-peaked structure do not have much in common with the 4 ML spectrum. This is another hint for the assumption that the rearrangement of Pd atoms, which undoubtedly occurs as a result of the considerable lattice mismatch, stays within the layers, as it is indicated by the Auger analysis, and does not produce a polycristalline volume which in general exhibits a fraction of roughly $\frac{2}{3}$ of (111) surfaces.

4.1.3. Photon energy dependence

A three-dimensional band structure in the direction normal to the sample surface can be measured in normal emission by varying the photon energy, i. e. taking spectra at different photon energies and determining the binding energies of a certain feature. This works, in the one-electron picture of band structure, because of the fact that in most cases the initial state band and the final state band disperse differently. Thus a given photon energy determines a transition at a certain $\mathbf{k}_\perp$ where Eq. 12 is satisfied. Variation of $h\nu$ changes $\mathbf{k}_\perp$ and enables to map the initial or the final state band if either one is known approximately.

On the contrary, a two-dimensional system like a monolayer or an interface does not possess a $\mathbf{k}_\perp$ dependent band structure and thus will not show a dispersion with the photon energy, unless it is not two-dimensional.

1±0.1 ML of Pd/Fe(100) has been prepared and tested in this sense. Inevitable is the knowledge of the Fe behavior which is shown in Fig. 27.

The $h\nu$ dependence of Fe(100) valence band spectra has been studied earlier by *Turner et al.* [97] They find the peak appearing in Fig. 27 close to E_F for 12 eV and 13 eV photon energy to derive from the $\Delta_5^\uparrow$ band which crosses the Fermi edge near the H point and thus causes the disappearance of the peak for photon energies above 14 eV. The peak that appears at about 0.5 eV binding energy for $h\nu = 13$ eV to 18 eV is attributed to surface emission from a region of the Brillouin zone with a high density of states, namely $\Gamma_{25}'^{\downarrow}$ and $\Gamma_{12}'^{\uparrow}$ [97]. The origin of the peak at 1.4 eV is not yet established.

Fig. 28 shows the photon energy dependence after deposition of 0.5±0.1 ML Pd. The vertical line marks the position of the Pd derived structure as it has, for better accuracy, been gained from spectra in which the Fe contribution had been subtracted (not shown). The structure below 2 eV binding energy in the spectra taken at $h\nu \leq 17$ eV is obviously due to emission from the underlying Fe.

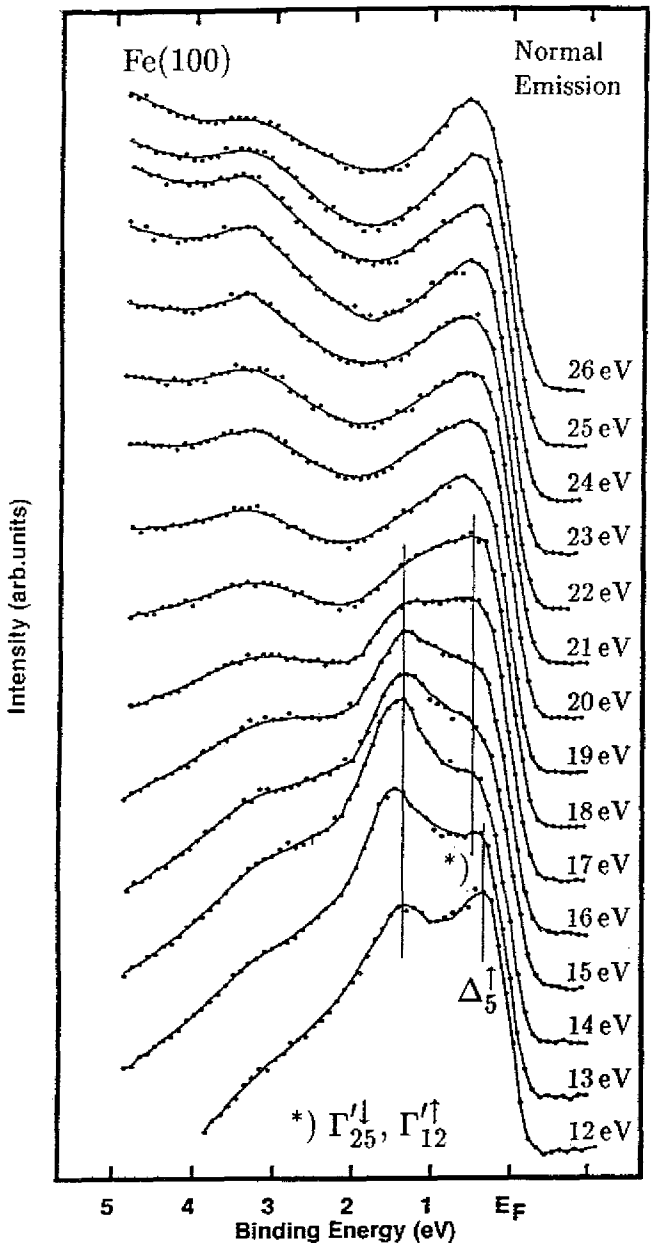

Fig. 27: Dependence of normal emission spectra from Fe(100) on the photon energy in the range $h\nu$=12 eV to 26 eV; s-polarization.

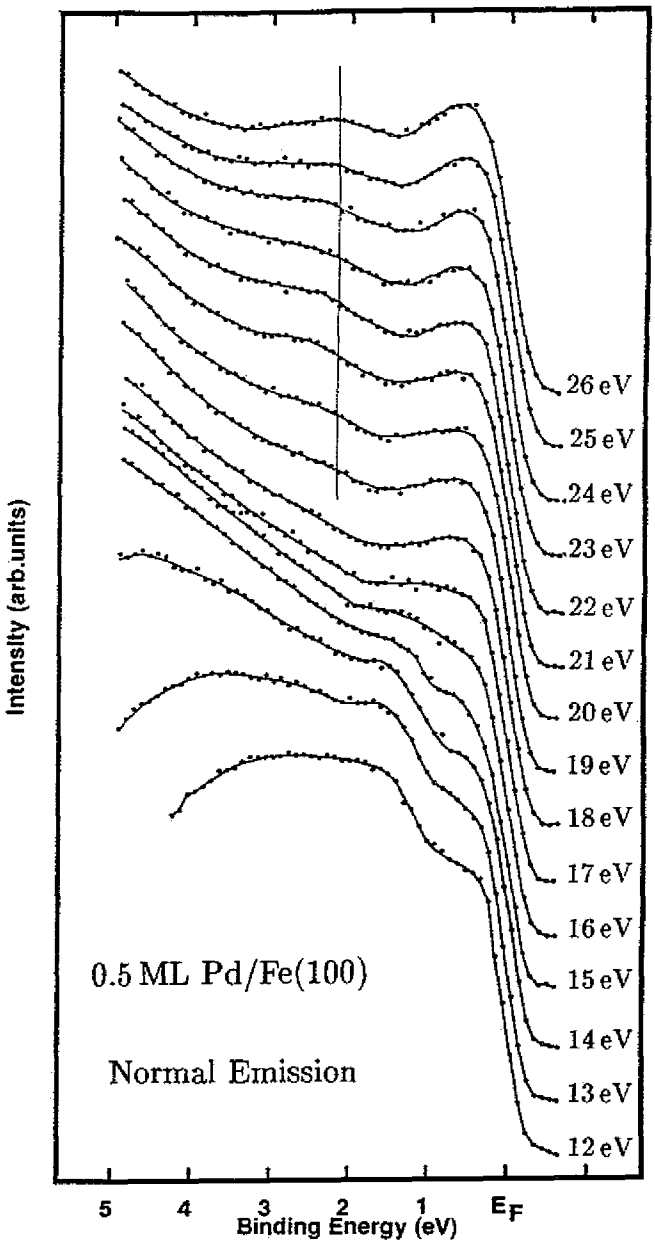

Fig. 28: Same as Fig. 27, but for 0.5±0.1 ML Pd/Fe(100).

Fig. 29 a) shows the same measurement performed with a coverage of 1±0.1 ML Pd. A vertical straight line marks the position where the maximum of the Pd emission is directly observed in the spectrum. The binding energy of the Pd derived feature, as obtained by subtracting the Fe (shown in Fig. 29 b), is denoted by a dotted line. The difference in position between both lines is in part a result of the increased background of inelastically scattered electrons in the Pd covered spectra.

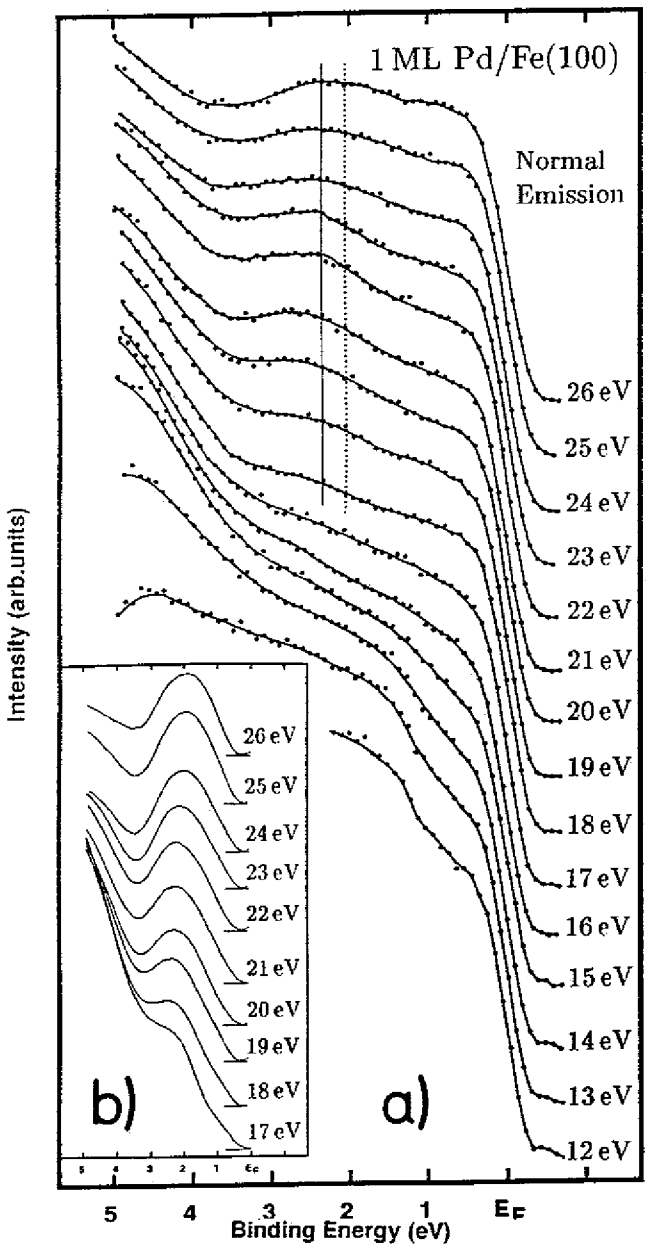

Fig. 29: a) Same as Fig. 27, but for 1±0.1 ML Pd/Fe(100). b) Smoothed subtraction of the Fe spectra in Fig. 27 from those shown in a).

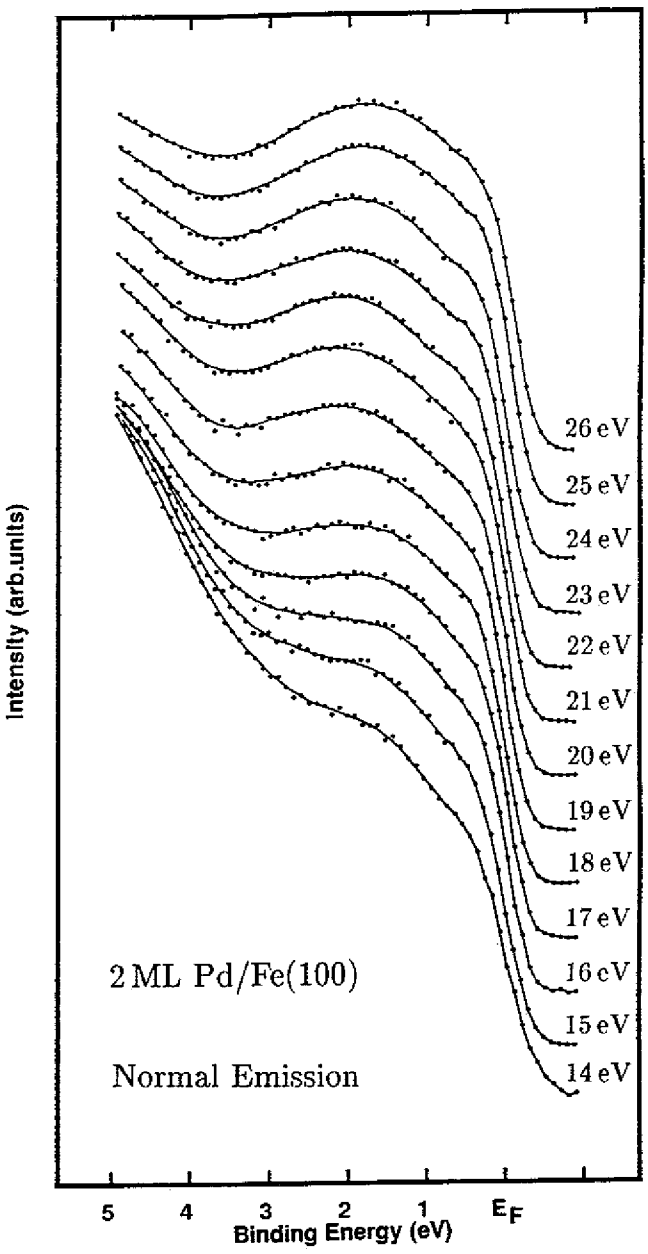

Fig. 30: Same as Fig. 27, but for 2±0.2 ML Pd/Fe(100) and $h\nu$=12 eV to 26 eV.

These remarks also hold true for the 2 ML spectrum which is displayed in Fig. 30.

In summary, a dispersion with $\mathbf{k}_\perp$ is not found in the photon energy range 19 to 26 eV. Thus the system behaves like a true two-dimensional phase.

4.1.4. Angle dependence

A band mapping in the two-dimensional Brillouin zone has been done for the Pd monolayer. The two high-symmetry directions in the surface Brillouin zone of the bcc lattice are the $\bar{\Gamma}$-$\bar{X}$ direction along the [010] and [001] axes of the three-dimensional lattice and the $\bar{\Gamma}$-$\bar{M}$ direction along the [011] and [0$\bar{1}$1] axes (Fig. 31).

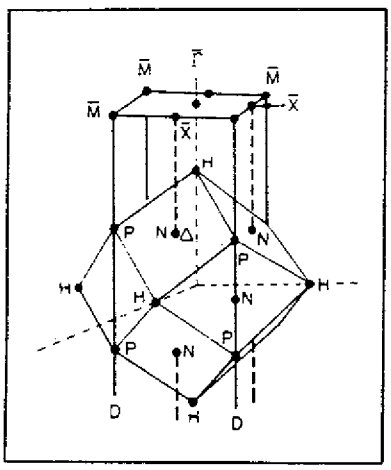

Fig. 31: Three-dimensional Brillouin zone of the bcc lattice and two-dimensional projection of the surface Brillouin zone. The high-symmetry directions in the surface Brillouin zone are the $\bar{\Gamma}$-$\bar{M}$ and the $\bar{\Gamma}$-$\bar{X}$ directions.

The lattice constant in reciprocal space is $\frac{2\pi}{a}$, therefore the $\bar{\Gamma}$-$\bar{M}$ distance $a_{\bar{\Gamma}\text{-}\bar{M}}$ amounts to $a_{\bar{\Gamma}\text{-}\bar{M}} = \frac{2\pi}{a} \cdot \frac{1}{\sqrt{2}} = \frac{\sqrt{2}\pi}{a}$. For a_{Fe} this is 1.548 Å^{-1}. The angle $\theta_{\bar{M}}$ by which the sample has to be turned off normal (Fig. 21) in order to arrive at $\bar{M}$ is determined by Eq. 10 in which $a_{\bar{\Gamma}\text{-}\bar{M}}$ has to be inserted for $\mathbf{k}_{\parallel}$. E_{kin} in Eq. 10 is defined by Eq. 5, where 2 eV, the binding energy of the peak in question, is inserted for E_B. Thus Eq. 10 yields $\theta_{\bar{M}} \approx 52°$. The sample has been mounted with [011] $\parallel$ **A** and turned around this axis in order to preserve *s*-polarization at any angle θ. θ was increased by steps of 10° from 0 to 50°, and the spectra obtained are shown in Fig. 32 a).

While in the range $\theta = 0°$ to 20° almost no change is visible, at 30° a broad feature can be found splitting off at the low binding energy side from the known Pd feature. At $\theta = 40°$ this feature has almost reached E_F where a determination of the energy position is difficult and it has crossed the Fermi level at the $\bar{M}$ point. Fig. 32 b) shows the behavior of both features as far as they can be followed in the spectra. The deviation in energy of the lower binding energy feature from the value 2 eV is due to the slope of the background as mentioned already in chap. 4.3.3, whereas band dispersion should remain unaffected by the background. Moreover, both features cannot be attributed to single transitions nor to distinct spin channels, but they are expected to be of odd symmetry because of *s*-polarization.

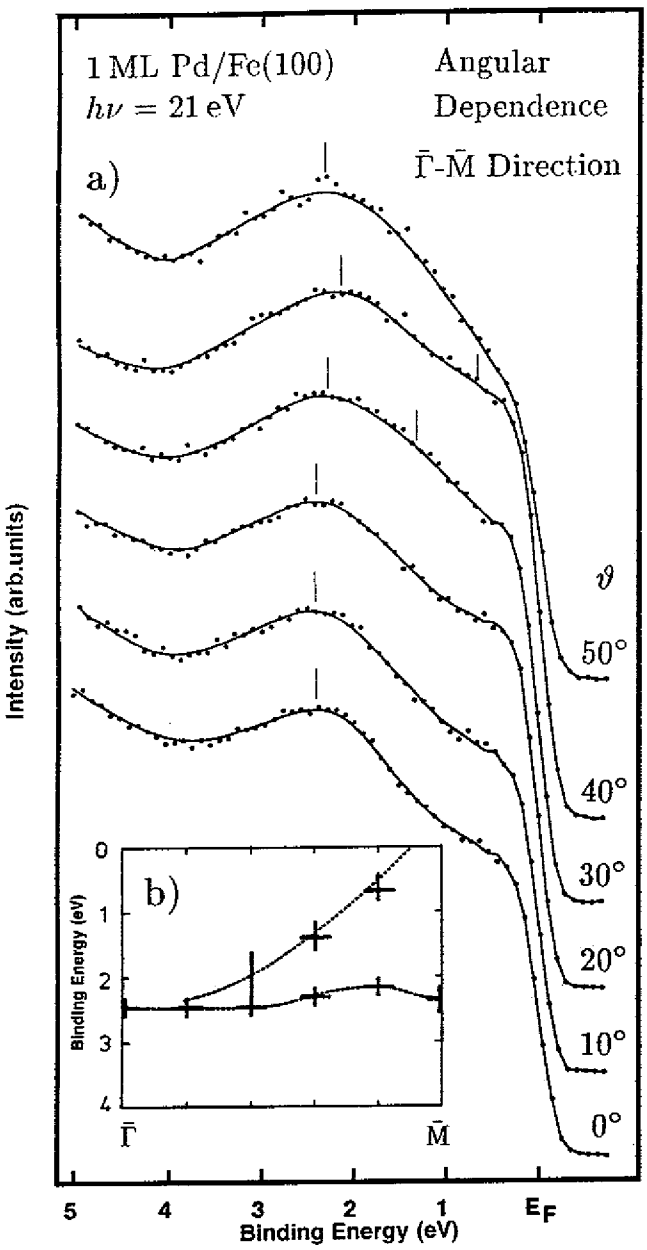

Fig. 32: (a) Angle-dependent spin-integrated spectra from 1±0.1 ML Pd/Fe(100). The wave vector $\mathbf{k}_{||}$ has been varied along the $\bar{\Gamma}$-$\bar{M}$ direction. The tilting axis of the sample is such that *s*-polarization is preserved at any angle θ. (b) Compilaton of the energy positions determined from (a) in a band structure plot.

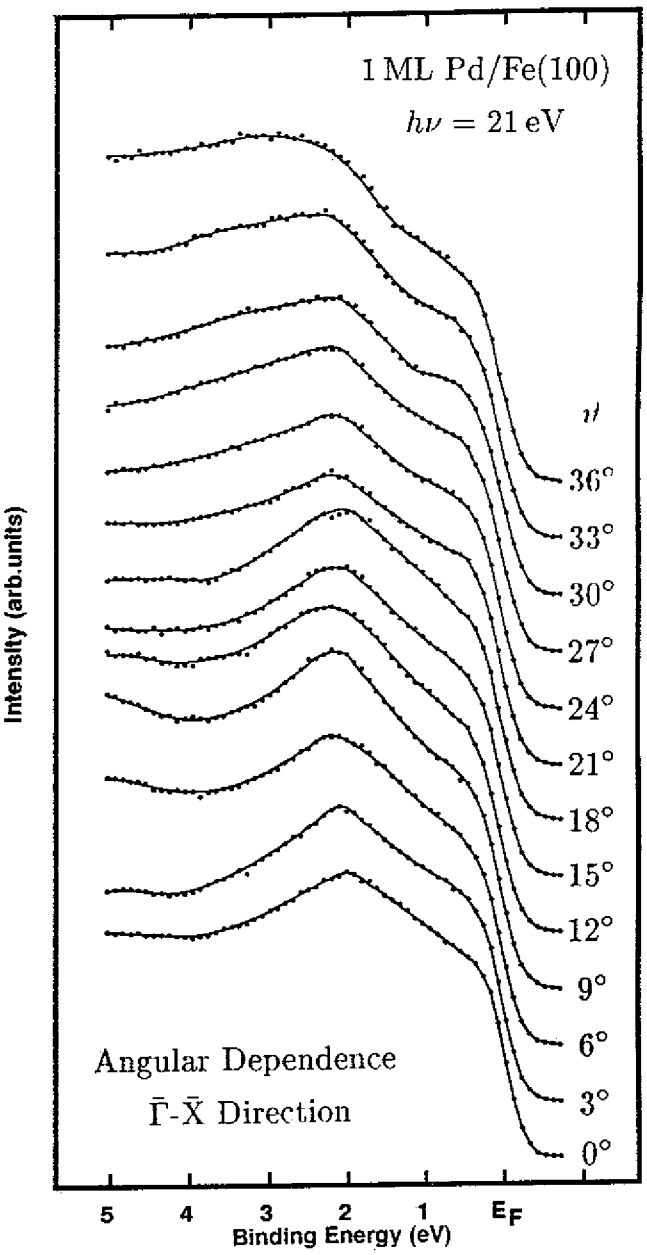

Fig. 33: Angle-dependent spin-integrated spectra from $1^{+0.2}_{-0.1}$ ML Pd. Pd/Fe(100). $\mathbf{k}_{||}$ varied along the $\bar{\Gamma}$-$\bar{X}$ direction. At small angles θ *s*-polarized light, at larger angles a small admixture of *p*-polarization.

Fig. 33 shows a compilation of spectra where $\mathbf{k}_{||}$ has been varied along the $\bar{\Gamma}$-$\bar{X}$ direction. In this case the coverage is $1^{+0.2}_{-0.1}$ ML Pd. According to the ratio $1:\sqrt{2}$ between $a_{\bar{\Gamma}\text{-}\bar{M}}$ and $a_{\bar{\Gamma}\text{-}\bar{X}}$, holds $\theta_{\bar{X}} \approx 36°$. Beyond $\theta = 18°$ a broad feature splits

off from the 2 eV feature to higher binding energy. Nevertheless, binding energies cannot be obtained. This measurement was performed with the sample mounted with its [010] direction parallel to the polarization vector, and it was tilted around its [001] axis so that at small angles θ we have s-polarized light whilst at larger angles a small admixture of p polarization has to be taken into account.

*4.2. Spin-resolved photoelectron spectroscopy**

4.2.1. The Fe substrate

A prerequisite for understanding the spin-resolved Pd/Fe(100) spectra is the discussion of the contributions from the substrate. Therefore in the following the results of earlier investigations of spin-resolved photoemission from Fe(100) are summarized.

A spin-resolved spectrum of the clean Fe is displayed in Fig. 34.

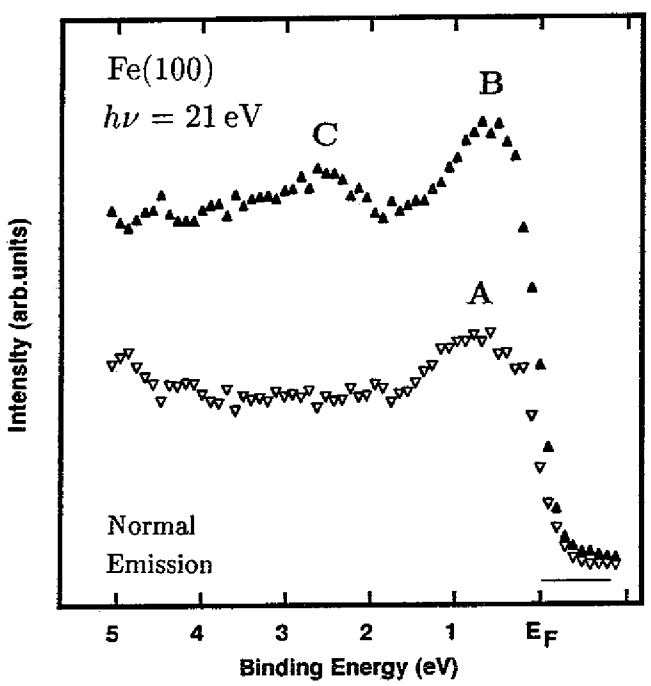

Fig. 34: Majority spin (▲) and minority spin (▽) valence band spectra at $h\nu$=21 eV and normal emission with s-polarized light from clean Fe(100).

The majority spectrum differs very much from the minority spectrum with respect to intensity, this means a high and positive spin polarization which is not limited to the valence band, but becomes even more pronounced for the secondary

* Spin-resolved photoelectron spectroscopy experiments have been reviewed by *Kisker* (Ref. 91) and *Kisker* and *Carbone* (Ref. 92).

electrons[84]. Three features are visible in the spectrum: either one peak near E_F in the minority channel — named **A** — and in the majority channel — named **B** — with the latter more pronounced and a broad but small majority peak **C** at about 2.5 eV binding energy.

As the experiment has been performed at normal emission on a bcc (100)-surface the direction we probe in varying $h\nu$ is the Δ direction leading from Γ to H. With *s*-polarized light we expect emission from odd states, here the Δ_5 band, as apparent from Tab. 1. Spin-resolved Fe band structure calculations[98,99] show that the $\Delta_5^{\uparrow}$ band crosses the Fermi energy close to the H point while the $\Delta_5^{\downarrow}$ band crosses E_F in the left half of the Γ-H direction. From this band structure one can gather that direct transitions at $h\nu = 21$ eV take place close to the H point[82]. The fact that at H the $\Delta_5^{\downarrow}$ band is already above E_F and that for its occupied part a Δ_1 final state is unaccessible by direct transitions at $h\nu = 21$ eV gives the reason for the rather featureless minority spectrum.

Kisker et al. [82] have published spin-resolved Fe(100) spectra at $h\nu = 20$, 21, 25, 31, 33, 35, 41, 50 and 70 eV and have observed that a majority spin peak around $E_B = 2.6$ eV is present at any photon energy. The question for this peak could only be answered after *Feder et al.* [100] had performed bulk band structure calculations (Fig. 35) and one-step photoemission calculations (Fig. 36) for photon energies from 20 to 70 eV.

They find that a minority spin feature **A** which corresponds to **A** in Fig. 34 stays at E_F at any photon energy (cf. left half of Fig. 36). As apparent from the calculated band structure[98,99,100] (Fig. 35) the $\Delta_5^{\downarrow}$ band is very flat below the Fermi energy. Besides other arguments the spin- and layer-resolved density of states[100] (not shown) provides evidence that **A** derives from this *bulk* $\Delta_5^{\downarrow}$ initial state[100]. According to *Feder et al.* the final state is a bulk band in the case of $h\nu = 20$ eV and a strongly attenuated LEED state for $h\nu \geq 31$ eV.

Also in the calculated majority spin spectra there is a peak (**B**) close to E_F that does not shift with the photon energy (Fig. 36). With the help of the layer density of states it is identified as a majority-spin *surface resonance* [100]. Another contribution to **B** may come from a direct transition from the $\Delta_5^{\uparrow}$ band near the H point ($H_{25}^{\prime\uparrow}$) into a $\Delta_1^{\uparrow}$ final state band. This transition is marked in Fig. 35 by a solid vertical arrow.

Eventually **C** at 2.5 eV derives from the same initial state band $\Delta_5^{\uparrow}$ as **B**. However, the final state belongs to a different free-electron parabola deriving from a different reciprocal-lattice vector component $\mathbf{g}_z$[100]. Dashed arrows denote this transition in Fig. 35, which occurs between 20 and 30 eV photon energy together with the transitions that result in **B**.

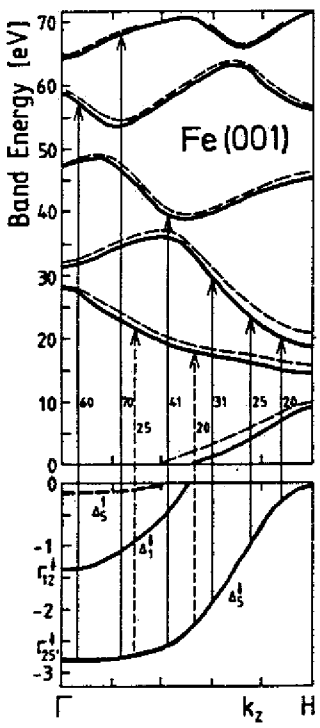

Fig. 35: Calculated Fe(100) bulk band structure for majority spin (—) and minority spin (---). Above E_F only Δ_1 symmetry bands are shown. (From Ref. 100)

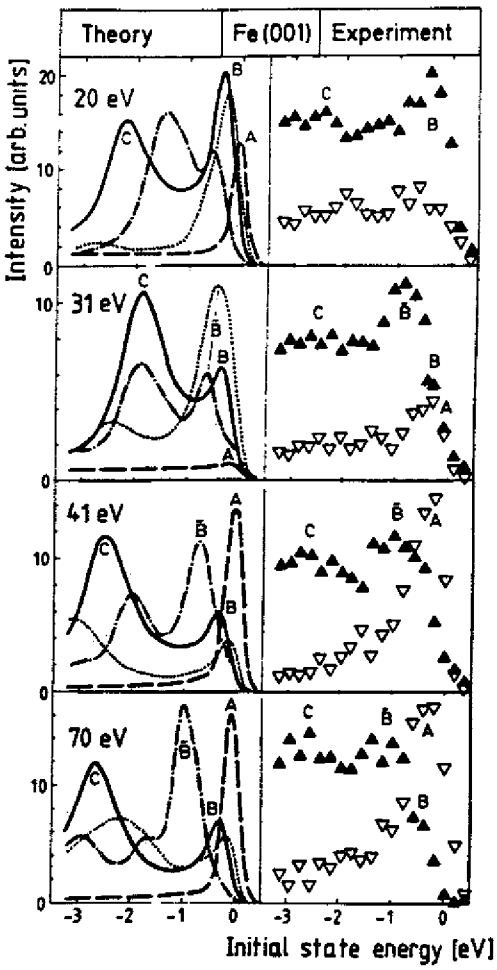

Fig. 36: Fe(100) photoemission spectra for s-polarized light and normal emission. Right hand: experimental majority spin (▲) and minority spin (▽) spectra from Ref. 82. Left hand: calculated majority spin (—) and minority spin (---) spectra for normal emission. A, B and C are explained in the text. (The peak denoted B̃ in the spectra for $h\nu \geq 31$ eV can be explained according to the 8°-off-normal emission spectra for $k_\parallel \| A$ (— · —) and $k_\parallel \perp A$ (· · ·) by a finite acceptance angle of the spectrometer). (From Ref. 100)

4.2.2. Pd coverage dependence

Fig. 37 shows a compilation of spin-resolved 21 eV spectra from Fe(100) covered with 0, 0.2±0.05, 0.4±0.1, 1±0.1, 1.3±0.1, 1.6±0.1, $2.1^{+0.2}_{-0.1}$, and 4±0.5 ML Pd.

The spin polarization at 3 eV binding energy, which can be taken as an average polarization of the valence band, decreases monotonously from (+37 ± 2)% for the

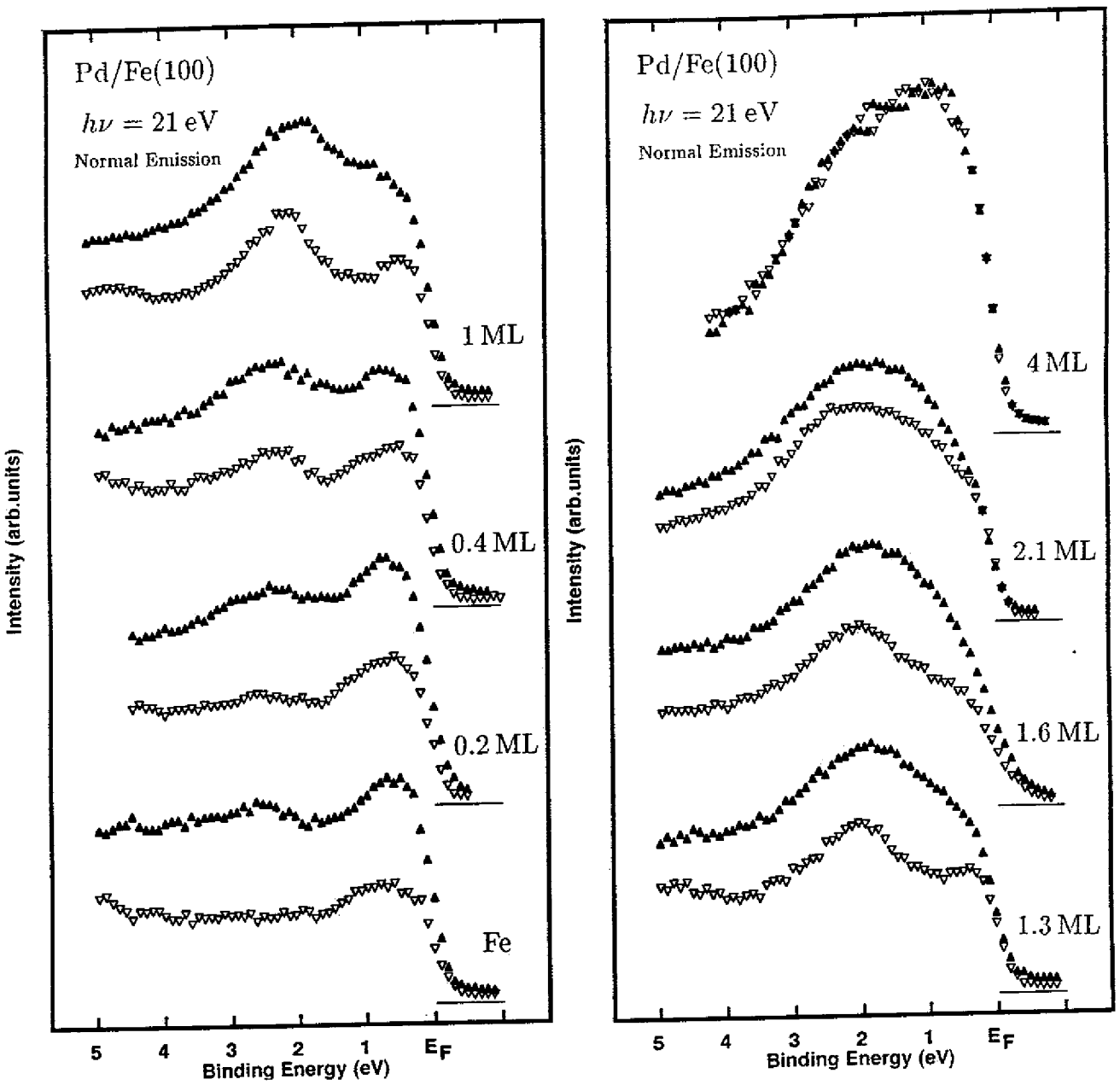

Fig. 37: Majority spin (▲) and minority spin (▽) valence band spectra at $h\nu$=21 eV and normal emission with s-polarized light from clean Fe(100) and Pd coverages of 0.2±0.05, 0.4±0.1, 1±0.1, 1.3±0.1, 1.6±0.1, $2.1^{+0.2}_{-0.1}$, and 4±0.5 ML.

clean Fe *via* +33% at 0.2 ML, +25% at 0.4 ML, +23% at 1 and 1.3 ML, +21% at 1.6 ML to become only +11% at 2.1 ML and +8% at ≈ 3 ML (not shown) and to vanish at ≈ 4 ML.

At 1 eV below E_F the spin polarization behaves in a different way. First it decreases from +28% for Fe to +26% for 0.2 ML and +21% for 0.4 ML. For one monolayer it exceeds with +30% the Fe value, remains high at 1.3 ML (+27%)

and 1.6 ML (+25%) and decreases to +10% at 2.1 ML and to zero for 4 ML. Residual polarization that appears to exist in the 4 ML spectrum is due to statistical scattering.

As the Fe *minority* spin spectrum is, in contrast to the majority channel, quite featureless, the first appearance of a Pd derived structure can be watched in the minority spin channel of the 0.2 ML spectrum. There a growing structure with its maximum at 2.6 eV binding energy can, in agreement with spin-integrated data, be attributed to emission from Pd. Furthermore, 0.4 to 0.6 eV away from E_F in the same minority spectrum the emission seems to be increased with respect to clean Fe. Both observations are confirmed by the 0.4 ML spectrum where in the minority channel the higher binding energy structure has shifted to about 2.3 eV while the lower binding energy feature stays at $\approx$ 0.5 eV. In the majority channel of the 0.4 ML spectrum a broad structure extending from 1.5 to almost 3.5 eV comes mostly from Pd emission whereas in the 0.2 ML spectrum it cannot be distinguished from Fe $\Delta_5^{\uparrow}$ emission. The majority-spin peak close to E_F seems to have decreased at 0.4 ML coverage which is not surprising provided it is predominantly due to Fe surface resonance emission.

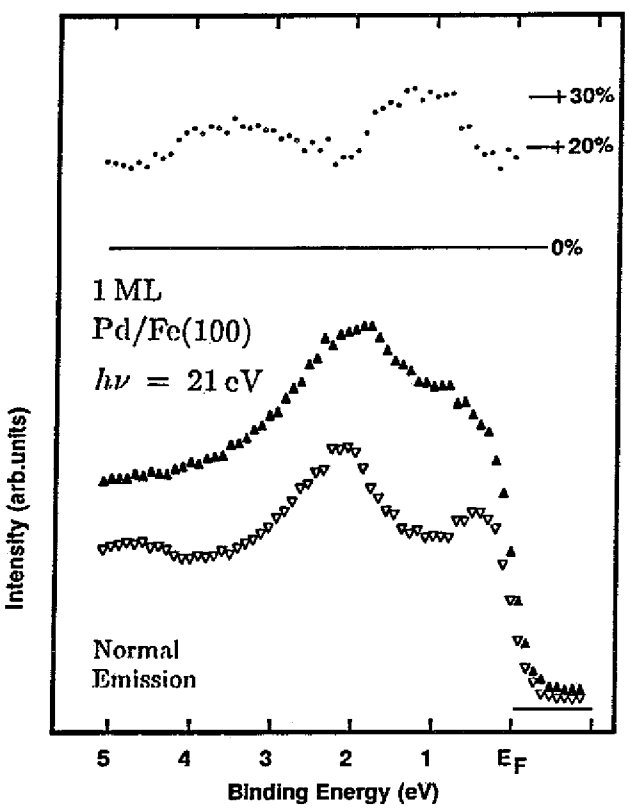

Fig. 38: Majority spin (▲) and minority spin (▽) valence band spectra and spin polarization (dots) at $h\nu$=21 eV and normal emission with *s*-polarized light from 1±0.1 ML Pd/Fe(100).

Concerning the *monolayer spectrum* (also shown in Fig. 38) strong differences can be observed between minority- and majority-spin emission. The minority channel is dominated by a comparatively sharp peak with its maximum at 2.1 eV.

The majority spectrum is more difficult to account for. It can be separated into at least three overlapping structures each manifesting itself by a shoulder. The positions of the shoulders are 2.3 eV, 1.75 eV and 0.8 eV.

Above 1 ML coverage changes in the spectra occur only in the range below 2 eV binding energy. At 1.3 ML the majority spin emission increases at around 1 eV thus smearing out the formerly separated shoulders of the monolayer spectrum. At 1.6 ML also the minority emission has noticeably increased around 1 eV. Eventually, during formation of the bulk more and more emission is transferred to lower binding energy.

4.3. Discussion

The energy shift of the minority spin feature from 2.6 eV at 0.2 ML to 2.1 eV at 1 ML is not surprising as Pd-Pd coordination is increased during Pd deposition. In this case the appearance and disappearance of two (or more) distinct structures would be a more appropriate description of the "shift".

The 4±0.5 ML spectrum shows no net spin-polarization. Keeping in mind that photoemission performed at this photon energy probes predominantly the first but also the second surface layer, this means that the fourth and likely also the third Pd layer in the system 4 ML Pd/Fe(100) is not polarized any more by the Fe. The fact that the spin polarization is considerably reduced after the completion of the second Pd layer (cf. the 2.1 ML spectrum) indicates that the second Pd layer in the 2 ML system is much less polarized by the Fe than the Pd layer at the interface. This is in qualitative agreement with the calculation for 1 ML Fe on Pd(100) by *Blügel*[8,11] who finds that magnetic moments of $0.32\mu_B$ and $0.17\mu_B$ are induced by the Fe overlayer on the first resp. second Pd layer while the moments of the underlying layers are negligible. Of course this comparison between a Pd layer at the surface and a Pd layer within the semi-infinite system Fe/Pd(100) with the same separation from the Fe/Pd interface does not allow quantitative conclusions. The same holds for a comparison with the already mentioned system of *Celinski et al.*[82] where all Pd atoms in the Fe/4Pd/Fe sandwich are reported to be ferromagnetic while those in Fe/5Pd/Fe are not[82].

The large spin polarization of the monolayer spectrum proves the existence of an induced moment in Pd. Yet, a pair of peaks, spin-split by the exchange interaction, such as known from the valence band emission from the ferromagnets Co[102] and Fe * cannot unambiguously be extracted from Fig. 38.

---

* For the Fe splitting see peaks A and C in the 70 eV spectrum of Fig. 36 and also Ref. 101. The results obtained from Ni (Ref. 103, Ref. 104, Ref. 105) are more complicated. For instance, an exchange splitting of only 0.18 eV has been measured, and it has been shown (Ref. 106) that this can be explained by correlations among the *d* electrons upon creation of the photoemission hole. However, the effect of correlation is expected to be smaller here than in

To support an interpretation in terms of a band structure model, *Blügel*[107] has performed a full-potential linearized augmented plane wave (FLAPW) calculation for a nine-layer Pd/7Fe/Pd slab simulating 1 ML Pd/Fe(100). The magnetic moment of the Fe at the Fe/Pd interface was found to be enhanced to $2.69\mu_B$ with respect to the central layer value of $2.01\mu_B$. The Pd atoms gain a moment of $0.29\mu_B$.[107]

A *paramagnetically* calculated Pd/7Fe(100)/Pd slab exhibits a surface density of states at E_F that is much too small to give rise to a stable ferromagnetic Pd phase.[107] Also a Pd monolayer on Ag(100), for which the lattice expansion (5.1%) is even larger than for Pd/Fe(100) (4.3%), has in a calculation been found to be paramagnetic by *Blügel*[110].

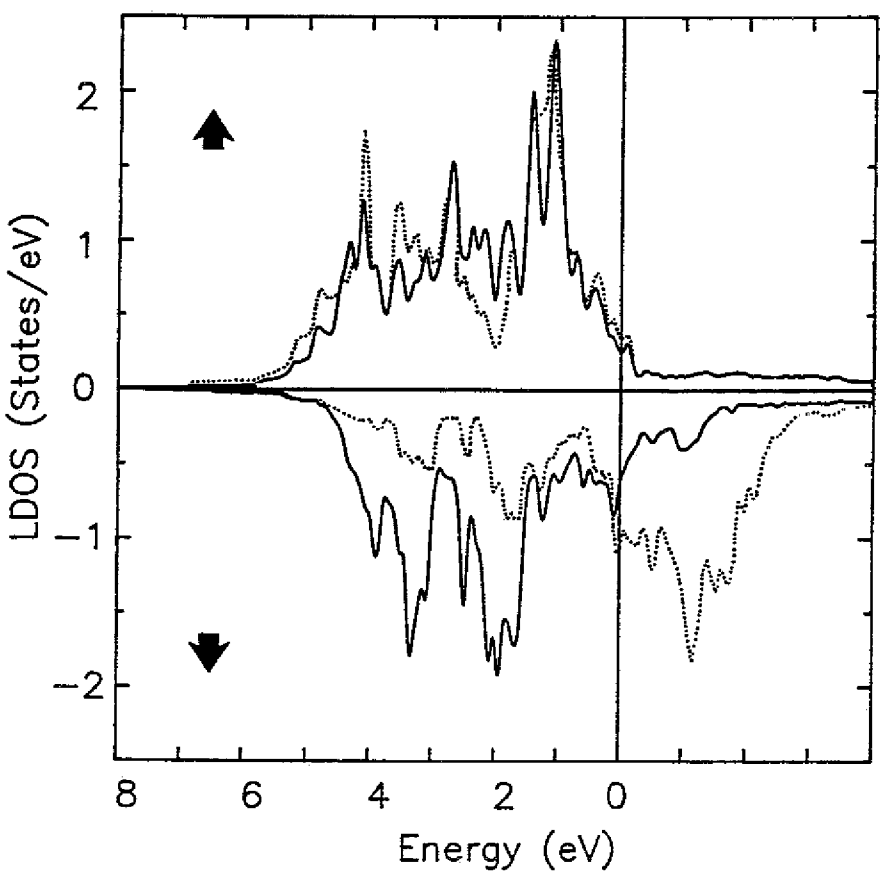

Fig. 39: Result of an FLAPW calculation for a Pd/7Fe/Pd slab by *Blügel* (Ref. 107): Layer-resolved majority-spin (↑) and minority spin (↓) density of states of the Pd overlayer on Fe(100) (solid line) and of the topmost Fe layer underneath the Pd (dotted line).

---

the case of Ni as, in general, correlations decrease with increasing principal quantum number, though, within the 4*d* series Pd must be regarded as the main candidate for this effect and the monolayer geometry should also promote it.

Fig. 39 shows the density of states (DOS) resulting from a ferromagnetic calculation at the site of the Pd overlayer (solid line). It looks completely different from that of Pd bulk[88]. In particular, the minority spin DOS of Fig. 39 is not simply a reproduction of the majority spin DOS shifted rigidly according to a Stoner model with constant exchange splitting. Instead, it exhibits essentially a double-peaked shape contrary to the triple-peaked majority DOS. The fact that majority and minority states are strongly different in the Pd overlayer is due to strong hybridization with the Fe substrate. This has earlier been noticed by *Huang et al.*[108] for a Pd/3Fe(100)/Pd slab, the DOS[108] of which looks similar to that of Fig. 39.

Already a comparison of calculated densities of states[88] of bulk Fe to bulk Pd shows that in the energy range between 0.5 and 3.5 eV below E_F for the *majority spin* direction Fe and Pd states are "overlapping" whilst for the *minority spin* direction and the same energy range only the Pd DOS is large because the Fe DOS is shifted across E_F by about 2 eV due to exchange. With regard to the Pd *overlayer* on Fe this indicates that 3*d*-4*d* hybridization is much stronger for majority spin electrons than for the minority electrons. The quantitative effect of this can be seen in Fig. 39 where the dotted line marks the DOS of the first underlying Fe layer. In the minority spin DOS there are only few Fe states the Pd can couple to. Therefore the majority spin Pd states are expected to be more strongly affected by hybridization with the Fe than the minority states.

The density of states is the result of an integration across the Brillouin zone. A comparison of angle-resolved photoemission spectra with a calculation, however, requires **k**-resolved band structure data. Of special interest is in this case the $\bar{\Gamma}$ point as the spin-resolved spectra were taken in normal emission geometry and thus at the center of the two-dimensional Brillouin zone of the Pd overlayer.

In Fig. 40 and Fig. 41 a spin-resolved band structure in the $\bar{\Gamma}$-$\bar{X}$ direction from *Blügel*[107] is plotted. Fig. 40 shows the minority spin direction and Fig. 41 the majority.

Distinction is also made between states of even and odd symmetry upon reflection about a mirror plane perpendicular to the surface.

In our experimental geometry (*s*-polarized light, normal emission) we expect emission from states at the center of the two-dimensional Brillouin zone that are antisymmetric with respect to rotation about the surface normal, i. e., $\bar{\Gamma}_5$. In the analysis of the calculated data we concentrate on those states whose wave functions lead to a high probability in Pd muffin-tin spheres for electronic states of $\bar{\Gamma}_5$ symmetry. This restriction to the Pd states is convenient as the theoretical predictions are compared to experimental data taken at a photon energy where the ionization cross section in 5.4 times larger for Pd than for Fe.

In this way occupied states with more than 10% Pd 4*d* character are found at 2.68, 1.83, 1.41, 0.95, and 0.45 eV binding energy for majority and at 1.57 eV for minority spin. These states are marked by dots in Fig. 40 and Fig. 41. A complete matching of the energies between theory and experiment is obtained when shifting the calculated majority and minority spin bands rigidly by 0.5 eV

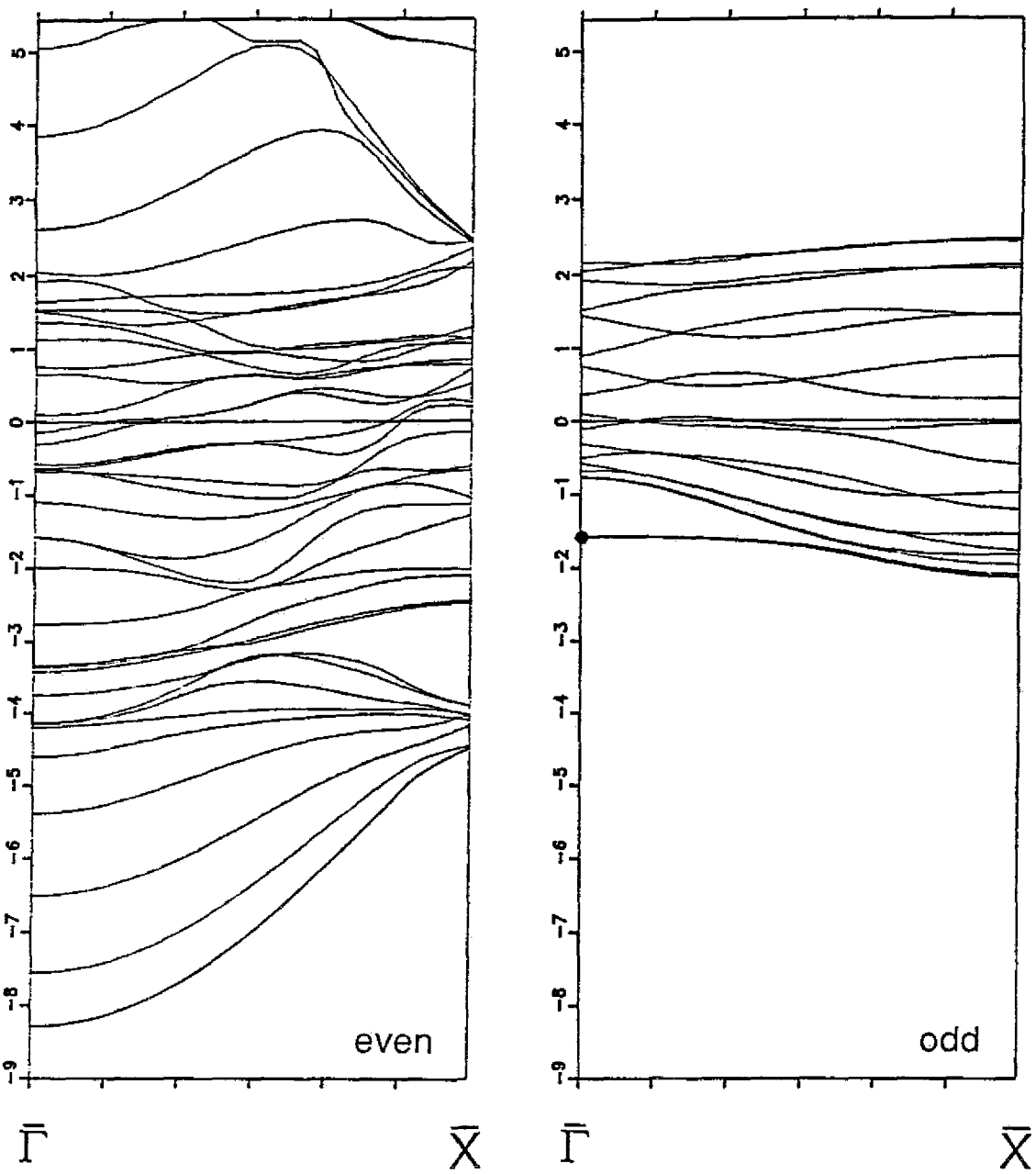

Fig. 40: Minority spin band structure for 1 ML Pd/Fe(100) in the $\bar{\Gamma}$-$\bar{M}$ and the $\bar{\Gamma}$-$\bar{X}$ directions after k- and layer-resolved data from *Blügel* (Ref. 107). "Even" and "odd" with respect to reflection upon a mirror plane perpendicular to the slab surface. States with most of their weight in the Pd layer are drawn with solid lines, other states dashed.

to higher binding energies. This was done in Fig. 42 and is typical of the comparison of experimental band structures with those obtained by *ab initio* methods

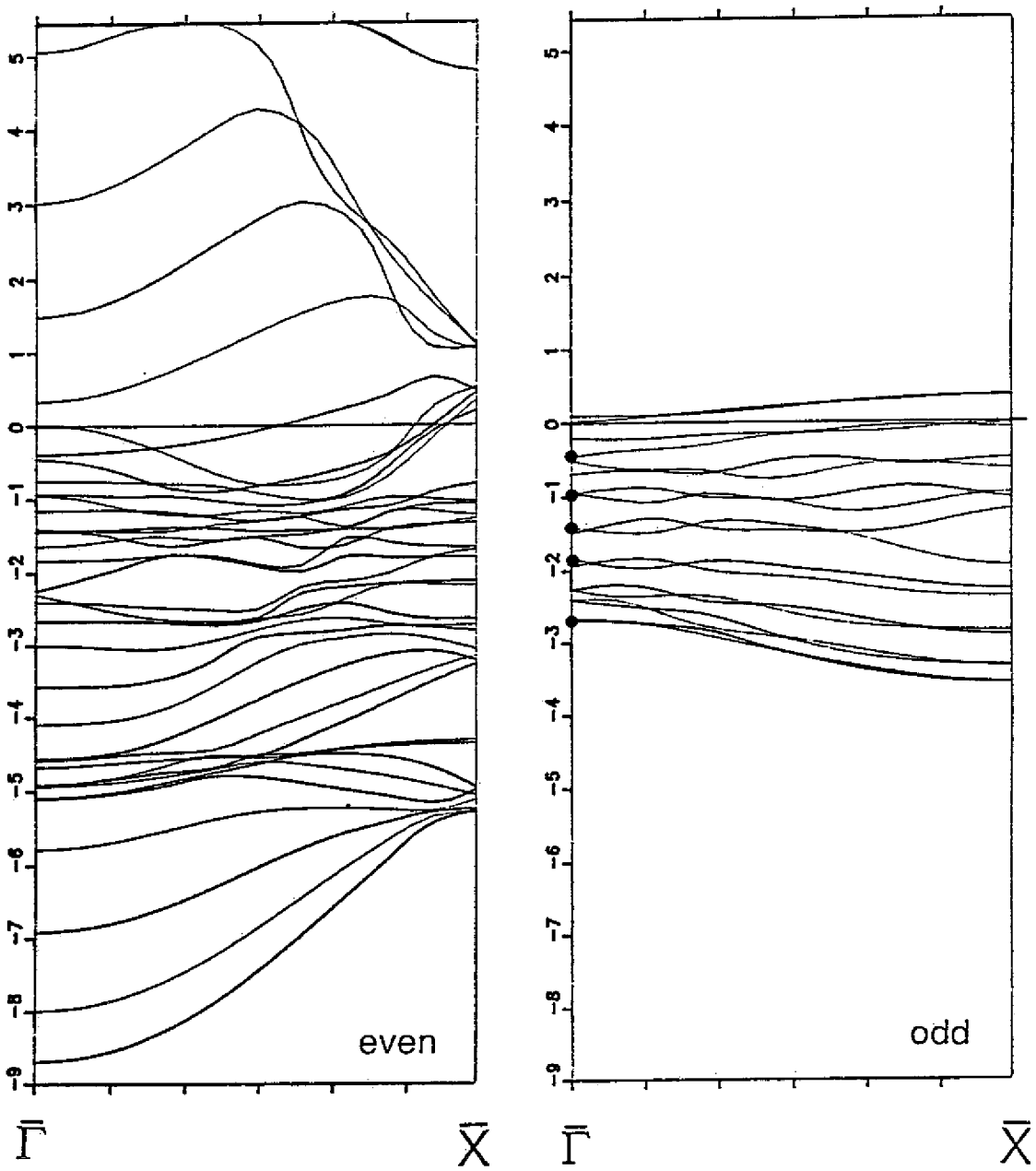

Fig. 41: Same as Fig. 40, but for the majority spin direction.

based on density functional theory. The pie charts of Fig. 42 contain, for the states in question, information on to which probability they are located at Pd sites. Obviously, only the $\bar{\Gamma}_5^{\downarrow}$ state identified with the peak at 2.1 eV is located by 87% at the Pd layer and therefore is of almost pure Pd 4*d* character. But in contrast to this deepest $\bar{\Gamma}_5^{\downarrow}$, the corresponding $\bar{\Gamma}_5^{\uparrow}$, exchange-split by +1.1 eV,

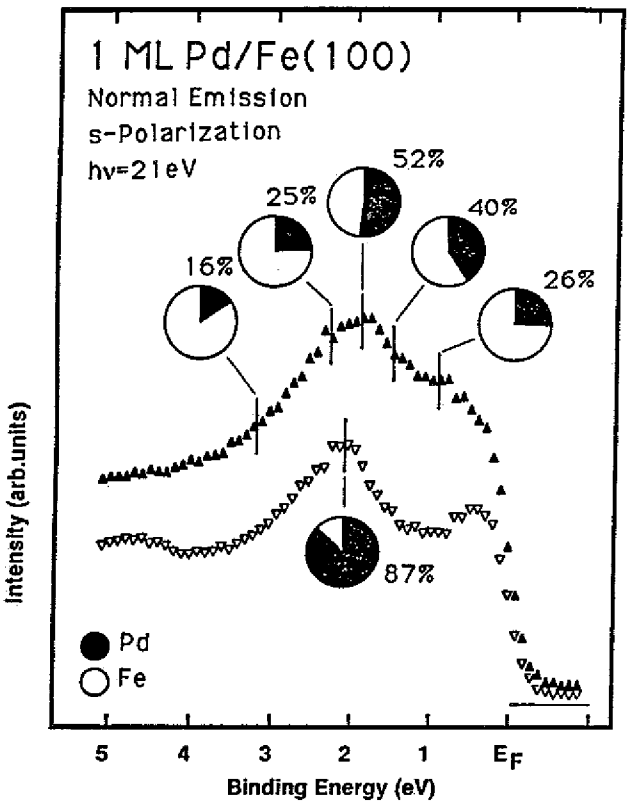

Fig. 42: Comparison between experiment and calculation: ▲ and ▽ are experimental data of 1 ML Pd/Fe(100) taken from Fig. 38. Vertical bars represent the energy positions of $\bar{\Gamma}_5$ states obtained from the *ab initio* calculation after a shift of 0.5 eV towards higher binding energy. The pie charts indicate the calculated amount of Pd character in percent. (States with less than 10% Pd character are not shown.)

shows due to the strong 4*d*-3*d* hybridization 84% Fe 3*d* character, which implies that for reasons of photoionization cross section this state is expected to be suppressed at 21 eV photon energy. On the other hand, the hybridization causes a distribution of the Pd character in the majority spin direction among the other $\bar{\Gamma}_5^{\uparrow}$ states at lower binding energies. These states obviously correspond to the shoulders at 0.8, 1.75, and 2.3 eV observed in the majority spin channel of the experimental spectrum.

After the termination of the experimental part of this work a report has been published in which *Weber et al.* [111] present results of spin-resolved photoemission from ultrathin Pd on Fe(110). For the system 1 ML Pd(111)/Fe(110) they surprisingly find a pair of Pd derived peaks with a splitting inverted with respect to that of Fe. Still, the question whether and how hybridization, as the authors suggested, can be identified as the origin of this structure could not be answered conclusively because the appropriate band structure calculation is unavailable. A different *magnetic structure*, i. e., antiferromagnetic coupling between overlayer and substrate, still appeared possible.

We have compared our experimental results to a calculation with regard to the correct geometry and location in **k** space and in consideration of selection rules. Thereby it has been shown that our experimental findings can be accounted for on the basis of the calculation.

5. Summary

The aim of this work has been to investigate the spin-polarized electronic structure of ultrathin layers of Pd on Fe(100). The motivation were the various hints for magnetism in the Pd overlayer based on an enhanced susceptibility at the Pd surface[12], the expansion of the Pd lattice[25-29,82], and the contact of Pd with Fe[13,17,81,82]. The possibility of interdiffusion between Fe and Pd in non-epitaxially grown systems[112] and the fact that FePd alloys behave ferromagnetically in a wide compositional regime[16] were the reasons for a careful sample preparation under best possible growth conditions and a thorough investigation of the growth mode by LEED and Auger electron spectroscopy. Pd was found to grow epitaxially on top of Fe(100) up to 2 ML thereby adopting the by 4.3% larger in-plane lattice constant of Fe. In-plane long-range order is lost during the growth of the third Pd layer. Layer by layer growth persists up to at least 5 ML. No indication for interdiffusion was found. An interdiffusion involving about $\frac{1}{5}$ ML Pd would have been recognized by the Auger analysis.

Spin- and angle-resolved photoemission from Pd overlayers on Fe(100) has been performed at 21 eV photon energy where Pd emission is favoured due to the larger ionization cross section with respect to Fe. The average valence band spin polarization amounts to (+23±2)% for 1 ML Pd/Fe(100) and decreases with increasing Pd coverage to vanish at 4±0.5 ML coverage. With regard to the probing depth it is concluded that a monolayer of Pd is polarized by the Fe, the second Pd layer in the system 2 ML Pd/Fe(100) is already much less polarized than the first, and the fourth and likely also the third layer in the system 4±0.5 ML Pd/Fe(100) are not any more polarized by the Fe.

The spin-resolved photoemission spectrum of 1±0.1 ML Pd/Fe(100) requires an accurate comparison to a band structure calculation. This comparison between the spectrum and an FLAPW calculation for a Pd/7Fe/Pd slab[107] has been conducted on the basis of identical geometry, angle resp. **k**-vector resolution, and a symmetry argument with regard to selection rules. The calculation proved to be consistent with angle-dependent spin-integrated spectra and describes the predominant features of the spin-resolved spectrum of 1 ML Pd/Fe(100), which are a broad majority spin structure with shoulders at about 2.3, 1.75, and 0.8 eV and a comparatively sharp minority spin peak at 2.1 eV binding energy. The FLAPW calculation shows that the Pd 4*d*-Fe 3*d* hybridization creates an electronic structure at the Pd-Fe interface that is two-fold: The minority spin electronic structure of the Pd is only little affected by hybridization with the Fe. In contrast, in the majority electronic structure the hybrdization leads to a spreading of the Pd 4*d* character among several states of identical symmetry. This is exactly reflected in the spin-resolved spectrum, where all of the predicted states appear, for reasons of cross section, according to their quantity of Pd 4*d* character.

Acknowledgements

This diploma thesis has been written at the *Institut Elektronische Eigenschaften* (IEE) within the *Institut für Festkörperforschung* of the *Forschungszentrum Jülich*. I should like to thank Prof. Wolfgang Gudat, now director at the synchrotron light source BESSY, for kind reception in the IEE. He has suggested this work and inspired it in many discussions. No less has Prof. Wolfgang Eberhardt, since he took over the direction of the IEE, supported this project.

I have participated from March 1990 until February 1991 in the spin-resolved photoemission activities of the IEE at BESSY in Berlin, at the beginning together with Dr. Torsten Kachel to whom I am grateful for introducing me to the performance of spin-resolved photoemission. The data presented in this work I have measured at the BESSY beamline TGM 1 between October and February and under the guidance of Dr. Carlo Carbone. I have profited very much from his experience and knowledge and I am obliged to him for his advice, encouragement, and patience. I like to thank Wolfgang Clemens who has also expended very much time on this work in the long measurement nights at BESSY. I had many helpful discussions with him and with Dr. Elio Vescovo, who joined this project later. Essential support to this work came from Dr. Stefan Blügel who conducted the FLAPW calculation. For this and for the many succeeding discussions we had I am extraordinarily thankful to him.

The instructions in LEED and Auger spectroscopy by Dipl.-Phys. Ralf Kersjes and in ultrahigh vacuum technique by Ing. Dieter Hoffmann and the support by the BESSY staff I also acknowledge gratefully. I thank Prof. E. Müller-Hartmann, chairman of the examination committee at the University of Cologne, for the permission to write this thesis in English and Prof. G. Dietz for his willingness to co-assess the thesis.

References

[1] J. W. Ritter, "Fragmente aus dem Nachlasse eines jungen Physikers", Kap. VIII (Mohr und Zimmer, Heidelberg 1810)

[2] W. Dürr, M. Taborelli, O. Paul, R. Germar, W. Gudat, D. Pescia, and M. Landolt, *Phys. Rev. Lett.* **62**, 206 (1989)

[3] W. Heinen, C. Carbone, T. Kachel, and W. Gudat, *J. Electr. Spectr. Relat. Phen.* **51**, 701 (1990)

[4] S. Blügel, private communication

[5] S. Foner, R. Dolco, and E. J. McNiff, Jr., *J. Appl. Phys* **39**, 551 (1968)

[6] T. Jarlborg and A. J. Freeman, *Phys. Rev. B* **23**, 3577 (1981)

[7] J. G. Gay, J .R. Smith, F. J. Arlinghaus, and T. W. Capehart, *Phys. Rev. B* **23**, 1559 (1981)

[8] S. Blügel, Thesis (RWTH Aachen) *Berichte der Kernforschungsanlage Jülich GmbH* Jül-2197 (1988)

[9] J. F. Janak, *Phys. Rev. B* **16**, 255 (1977)

[10] O. Gunnerson, *J. Phys. F* **6**, 587 (1976)

[11] S. Blügel, B. Drittler, R. Zeller, and P. H. Dederichs, *Appl. Phys. A* **49**, 457 (1989)

[12] G. Bergmann and G. Mathon, *Solid State Commun.* **56**, 881 (1985)

[13] G. J. Nieuwenhuys, *Adv. Phys.* **24**, 515 (1975)

[14] Latest theoretical results on 3d impurities in Pd can be found in J. F. van Acker, W. Speier, and R. Zeller, *Phys. Rev. B* **43**, 9558 (1991) and refs. therein.

[15] see e. g. J. A. Mydosh and G. J. Nieuwenhuys in E. P. Wohlfarth (ed.), "Ferromagnetic Materials" Vol. 1, 71 (North-Holland, Amsterdam 1980)

[16] M. Matsui, T. Shimizu, H. Yamada, and K. Adachi, *J. Magn. Magn. Mat.* **15-18**, 1201 (1980)

[17] B. Hillebrands, A. Boufelfel, C. M. Falco, P. Baumgart, G. Güntherodt, E. Zirngiebl, and J. D. Thompson, *J. Appl. Phys.* **63**, 3880 (1988)

[18] J. C. Ododo, *J. Phys. F* **13**, 1291 (1983)

[19] N. Hosoito, T. Shinjo, and T. Takada, *J. Phys. Soc. Jpn.* **50**, 1903 (1981)

[20] T. Shinjo, N. Hosoito, and T. Takada, *J. Magn. Magn. Mat.* **31-34**, 879 (1983)

[21] Y. Endoh, H. Ono, N. Hosoito, and T. Shinjo, *J. Magn. Magn. Mat.* **31-34**, 881 (1983)

[22] N. Hosoito, K. Kawaguchi, T. Shinjo, T. Takada, and Y. Endoh, *J. Phys. Soc. Jpn.* **53**, 2659 (1984)

[23] Comment to Ref. 22 by N. K. Jaggi and L. H. Schwartz, *J. Phys. Soc. Jpn.* **54**, 1652 (1985)

[24] Reply to Ref. 23 by T. Shinjo, N. Hosoito, and Y. Endoh, *J. Phys. Soc. Jpn.* **54**, 1654 (1985)

[25] V. L. Moruzzi and P. M. Marcus, *Phys. Rev. B* **39**, 471 (1989)

[26] L. Fritsche, J. Noffke, and H. Eckardt, *J. Phys. F* **17**, 943 (1987)

[27] H. Chen, N. E. Brener, and J. Callaway, *Phys. Rev. B* **40**, 1443 (1989)

[28] M. B. Brodsky and A. J. Freeman, *Phys. Rev. Lett.* **45**, 133 (1980)

[29] C. Rau (Seminar at FU Berlin, 1990)

[30] R. L. Fink, C. A. Ballentine, J. L. Erskine, and J. A. Araya-Pochet, *Phys. Rev. B* **41**, 10175 (1990)

[31] B. Hillebrands, P. Baumgart, and G. Güntherodt *Appl. Phys. A* **49**, 589 (1989)

[32] Z. Celinski, B. Heinrich, J. F. Cochran, W. B. Muir, A. S. Arrott, and J. Kirschner, *Phys. Rev. Lett.* **65**, 1156 (1990)

[33] see e. g. D. D. Sarma, C. Carbone, P. Sen, R. Cimino, and W. Gudat, *Phys. Rev. Lett.* **66**, 967 (1991)

[34] M. P. Seah and W. A. Dench, *Surf. Interface Anal.* **1**, 2 (1979)

[35] M. P. Seah in D. Briggs and M. P. Seah (edd.) "Practical Surface Analysis by Auger and X-ray Photoelectron Spectroscopy", 181 (John Wiley&Sons, Chichester 1983)

[36] P. Auger, J. Phys. Radium **6**, 205 (1925)

[37] L. A. Harris, *J. Appl. Phys.* **39**, 1419 and 1428 (1968)

[38] R. E. Weber and W. T. Peria, *J. Appl. Phys.* **38**, 4355 (1967)

[39] J. G. Dash, "Films on Solid Surfaces — The Physics and Chemistry of Physical Adsorption", chap. 8 (Academic Press, New York 1975) and refs. therein

[40] J. H. van der Merwe in H. G. Schneider and V. Ruth (edd.) "Advances in Epitaxy and Endotaxy", 129 (VEB Deutscher Verlag für Grundstoffindustrie, Leipzig 1971)

[41] R. Germar, W. Dürr, J. W. Krewer, D. Pescia, and W. Gudat, *Appl. Phys. A* **47**, 393 (1988)

[42] M. Volmer, "Kinetik der Phasenbildung" (Steinkopf, Dresden 1939)

[43] see Ref. 46 and refs. therein

[44] J. W. Sachtler, M. A. Van Hove, J. P. Biberian, and G. A. Somorjai, *Surf. Sci.* **110**, 19 (1981)

[45] I. N. Stranski and L. Krastanov, *Sitzber. der Akademie der Wissenschaften Wien, Math.-Naturw. Kl. Abt. II B* **146**, 797 (1938)

[46] J. A. Venables, G. D. T. Spiller, and M. Hanbücken, *Rep. Prog. Phys.* **47**, 399 (1984)

[47] E. Bauer, H. Poppa, and G. Todd, *Thin Solid Films* **28**, 19 (1975)

[48] W. Schlenk and E. Bauer, *Surf. Sci.* **93**, 9 (1980)

[49] C. Argile and G. E. Rhead, *Thin Solid Films* **87**, 265 (1982)

[50] S. Ossicini, R. Memeo, and F. Ciccacci, *J. Vac. Sci. Technol. A* **3**, 387 (1985)

[51] E. Bauer, H. Poppa, G. Todd, and F. Bonczek, *J. Appl. Phys.* **45**, 5164 (1974)

[52] S. H. Lu, Z. Q. Wang, S. C. Wu, C. K. C. Lok, J. Quinn, Y. S. Li, D. Tian, F. Jona, and P. M. Marcus, *Phys. Rev. B* **37**, 4296 (1988)

[53] C. J. Davisson and C. H. Kunsman, *Science* **52**, 522 (1921)

[54] C. J. Davisson and L. H. Germer, *Phys. Rev.* **30**, 705 (1927)

[55] J. J. Lander, F. Unterwald, and J. Morrison, *Rev. Sci. Instr.* **33**, 784 (1962)

[56] A. Einstein, *Ann. Phys.* **17**, 132 (1905)

[57] see e. g. E. W. Plummer and W. Eberhardt in I. Prigogone and S. A. Rice (edd.), "Advances in Chemical Physics", Vol. 49, 533 (John Wiley&Sons, New York 1982)

[58] see e. g. A. Liebsch in W. Gudat (ed.), "18. IFF-Ferienkurs: Synchrotronstrahlung in der Festkörperforschung" (Jülich 1987)

[59] E. O. Kane, *Phys. Rev. Lett.* **12**, 97 (1964)

[60] H. Y. Fan, *Phys. Rev. B* **68**, 43 (1945)

[61] H. Mayer, H. Thomas, *Z. Phys.* **147**, 419 (1957)

[62] W. E. Spicer, *Phys. Rev.* **112**, 114 (1958)

[63] H. Puff, *Phys. Stat. Solidi* **1**, 636 (1961)

[64] C. N. Berglund and W. E. Spicer, *Phys. Rev. A* **136**, 1030 and 1044 (1964)

[65] E. W. Plummer in R. Gomer (ed.), "Topics in Applied Physics", Vol. 4 (Springer, New York 1975)

[66] P. Thiry, Thesis (french), Université Pierre et Marie Curie (Paris 1981)

[67] P. J. Feibelman and D. E. Eastman, *Phys. Rev. B* **10**, 4932 (1974)

[68] S. G. Louie, P. Thiry, R. Pinchaux, Y. Petroff, D. Chandesris, and J. Lecante, *Phys. Rev. Lett.* **44**, 549 (1980)

[69] A. Liebsch, *Phys. Rev. Lett.* **32**, 1203 (1974)

[70] A. Liebsch, *Phys. Rev. B* **13**, 544 (1976)

[71] A. Liebsch, *Phys. Rev. Lett.* **38**, 248 (1977)

[72] A. Liebsch, *Solid State Commun.* **19**, 1193 (1976)

[73] W. Schaich and N. W. Ashcroft, *Phys. Rev. B* **3**, 2452 (1971)

[74] see e. g. J. B. Pendry in B. Feuerbacher, B. Fitton, and R. F. Willis (edd.) "Photoemission and the Electronic Properties of Surfaces" (John Wiley&Sons, Chichester 1978)

[75] G. D. Mahan, *Phys. Rev. B* **2**, 4334 (1970)

[76] J. Hermanson, *Solid State Commun.* **22**, 9 (1977)

[77] W. Eberhardt and F. J. Himpsel, *Phys. Rev. B* **21**, 5572 (1980)

[78] K. Siegbahn, C. Nordling, A. Fahlmann, R. Nordberg, K. Hamrin, J. Hedman, G. Johansson, T. Bergmark, S. Karlsson, I. Lindgren, and B. Lindberg, "ESCA — Atomic, Molecular and Solid State Structure Studied by Means of Electron Spectroscopy" (Almquist&Wiksells, Uppsala 1967)

[79] D. W. Turner and M. I. AlJoboury, *J. Chem. Phys.* **37**, 3007 (1962)

[80] D. Roy and J. D. Carette in H. Ibach (ed.) "Electron Spectroscopy for Surface Analysis", Topics in Current Physics, Vol. 4, 1 (Springer, Berlin 1977)

[81] W. Gudat, E. Kisker, K. Schröder, and M. Campagna, *Nucl. Instr. Meth. A* **208**, 809 (1983)

[82] E. Kisker, K. Schröder, W. Gudat, and M. Campagna, *Phys. Rev. B* **31**, 329 (1985)

[83] E. Kisker, W. Gudat, E. Kuhlmann, R. Clauberg, and M. Campagna, *Phys. Rev. Lett.* **45**, 2053 (1980)

[84] E. Kisker, W. Gudat, and K. Schröder, *Solid State Commun.* **44**, 591 (1982)

[85] D. P. Pappas, K. P. Kämper, B. P. Miller, H. Hopster, D. E. Fowler,

C. R. Brundle, A. C. Luntz, and Z. X. Shen, *Phys. Rev. Lett.* **66**, 504 (1991); *Verhandl. DPG (VI)* **26**, 1224 (1991) (German)

[86] J. Kessler, "Polarized Electrons" (Springer, Heidelberg 1985)

[87] N. F. Mott, *Proc. Roy. Soc. A* **124**, 425 (1929)

[88] see e. g. M. Campagna, F. Meier, D. T. Pierce, K. Sattler, and H. C. Siegmann in L. Dobrzynski (ed.), "Handbook of Surfaces and Interfaces", Vol. 1, 199 (Garland, New York 1978)

[89] G. Holtzwarth and H. J. Meister, *Nucl. Phys.* **59**, 56 (1964)

[90] G. Busch, M. Campagna, and H. C. Siegmann, *J. Appl. Phys.* **41**, 1944 (1970)

[91] E. Kisker in R. Feder (ed.), "Polarized Electrons in Surface Physics", 513 (World Scientific, Singapore 1985)

[92] E. Kisker and C. Carbone, to be published in S. D. Kevan (ed.) "Angle-resolved Photoemission" (Pergamon)

[93] J. J. Yeh and I. Lindau, *At. Data Nuc. Data Tab.* **32**, 1 (1985)

[94] D. R. Lloyd, C. M. Quinn, and N. V. Richardson, *Surface Sci.* **63**, 174 (1977)

[95] M. Pessa, M. Vulli and H. Asonen, *Ann. Isr. Phys. Soc.* **6**, 342 (1984)

[96] H. Conrad, G. Ertl, J. Küppers, and E. E. Latta, *Faraday Disc. Chem. Soc.* **58**, 116 (1974)

[97] A. M. Turner, A. W. Donoho, and J. L. Erskine, *Phys. Rev. B* **29**, 2986 (1984)

[98] V. L. Moruzzi, J. F. Janak, and A. R. Williams, "Calculated Electronic Properties of Metals" (Pergamon, New York 1978)

[99] J. Callaway and C. S. Wang, *Phys. Rev. B* **16**, 2095 (1977)

[100] R. Feder, A. Rodriguez, U. Baier, and E. Kisker, *Solid State Commun.* **52**, 57 (1984)

[101] E. Kisker, K. Schröder, M. Campagna, and W. Gudat, *Phys. Rev. Lett.* **52**, 2285 (1984)

[102] G. A. Prinz, E. K. Kisker, K. B. Hathaway, K. Schröder, and K. H. Walker, *J. Appl. Phys.* **57**, 3024 (1985)

[103] R. Raue, H. Hopster, and R. Clauberg, *Phys. Rev. Lett.* **50**, 1623 (1983)

[104] H. Hopster, R. Raue, E. Kisker, M. Campagna, and G. Güntherodt, *Phys. Rev. Lett.* **50**, 70 (1983)

[105] D. E. Eastman, F. J. Himpsel, and J. A. Knapp, *Phys. Rev. Lett.* **44**, 95 (1980)

[106] A. Liebsch, *Phys. Rev. Lett.* **43**, 1431 (1979)

[107] S. Blügel, to be published

[108] H. Huang, J. Hermanson, J. G. Gay, R. Richter, and J. R. Smith, *Surf. Sci.* **172**, 363 (1986)

[109] J. Noffke, W. Brunn, and K. Hermann, *Z. Phys.* **29**, 353 (1978)

[110] S. Blügel, to be published in *Europhys. Lett.*

[111] W. Weber, D. A. Wesner, G. Güntherodt, and U. Linke, *Phys. Rev. Lett.* **66**, 942 (1991)

[112] see Ref. 19 in comparison with Ref. 23, Ref. 24, Ref. 22

FORSCHUNGSZENTRUM JÜLICH GmbH

KFA

Jül-2558
November 1991
ISSN 0366-0885